



The Detection of Deuterated Water in the Large Magellanic Cloud with ALMA

Marta Sewiło^{1,2,3} , Agata Karska⁴ , Lars E. Kristensen⁵ , Steven B. Charnley⁶ , C.-H. Rosie Chen⁷ , Joana M. Oliveira⁸ , Martin Cordiner^{6,9} , Jennifer Wiseman¹ , Álvaro Sánchez-Monge¹⁰ , Jacco Th. van Loon⁸ , Remy Indebetouw^{11,12} ,

Peter Schilke¹⁰ , and Emmanuel Garcia-Berrios^{6,9,13}

¹ Exoplanets and Stellar Astrophysics Laboratory, NASA Goddard Space Flight Center, Greenbelt, MD 20771, USA; marta.m.sewilo@nasa.gov

² Department of Astronomy, University of Maryland, College Park, MD 20742, USA

³ Center for Research and Exploration in Space Science and Technology, NASA Goddard Space Flight Center, Greenbelt, MD 20771, USA

⁴ Institute of Astronomy, Faculty of Physics, Astronomy and Informatics, Nicolaus Copernicus University, ul. Grudziadzka 5, 87-100 Toruń, Poland

⁵ Niels Bohr Institute, Centre for Star & Planet Formation, University of Copenhagen, Øster Voldgade 5-7, DK-1350 Copenhagen K, Denmark

⁶ Astrochemistry Laboratory, NASA Goddard Space Flight Center, Greenbelt, MD 20771, USA

⁷ Max-Planck-Institut für Radioastronomie, Auf dem Hügel 69, D-53121 Bonn, Germany

⁸ Lennard-Jones Laboratories, Keele University, ST5 5BG, UK

⁹ Institute for Astrophysics and Computational Sciences, The Catholic University of America, Washington, DC 20064, USA

¹⁰ I. Physikalisches Institut der Universität zu Köln, Zülpicher Str. 77, D-50937, Köln, Germany

¹¹ Department of Astronomy, University of Virginia, PO Box 400325, Charlottesville, VA 22904, USA

¹² National Radio Astronomy Observatory, 520 Edgemont Rd, Charlottesville, VA 22903, USA

¹³ Department of Astronomy, University of Illinois, 1002 W. Green St., Urbana, IL 61801, USA

Received 2022 March 4; revised 2022 April 29; accepted 2022 May 6; published 2022 July 5

Abstract

We report the first detection of deuterated water (HDO) toward an extragalactic hot core. The HDO $2_{11}-2_{12}$ line has been detected toward hot cores N 105–2 A and 2 B in the N 105 star-forming region in the low-metallicity Large Magellanic Cloud (LMC) dwarf galaxy with the Atacama Large Millimeter/submillimeter Array (ALMA). We have compared the HDO line luminosity (L_{HDO}) measured toward the LMC hot cores to those observed toward a sample of 17 Galactic hot cores covering three orders of magnitude in L_{HDO} , four orders of magnitude in bolometric luminosity (L_{bol}), and a wide range of Galactocentric distances (thus metallicities). The observed values of L_{HDO} for the LMC hot cores fit very well into the L_{HDO} trends with L_{bol} and metallicity observed toward the Galactic hot cores. We have found that L_{HDO} seems to be largely dependent on the source luminosity, but metallicity also plays a role. We provide a rough estimate of the H_2O column density and abundance ranges toward the LMC hot cores by assuming that HDO/ H_2O toward the LMC hot cores is the same as that observed in the Milky Way; the estimated ranges are systematically lower than Galactic values. The spatial distribution and velocity structure of the HDO emission in N 105–2 A is consistent with HDO being the product of the low-temperature dust grain chemistry. Our results are in agreement with the astrochemical model predictions that HDO is abundant regardless of the extragalactic environment and should be detectable with ALMA in external galaxies.

Unified Astronomy Thesaurus concepts: Star formation (1569); Astrochemistry (75); Magellanic Clouds (990); Chemical abundances (224); Star forming regions (1565); Protostars (1302)

1. Introduction

Water (H_2O) is a key molecule tracing the chemical and physical processes associated with the formation of stars and planets. Water shows large abundance variations in star-forming regions because it can be produced in both the gas phase and on the surfaces of interstellar dust grains (e.g., van Dishoeck et al. 2021). In cold molecular gas, most water is in the form of ice, with only trace amounts in the gas. In outflow shocks where $T > 300$ K, water is predominantly in the gas phase where it forms directly (e.g., Suutarinen et al. 2014; Kristensen et al. 2017; Karska et al. 2018). Deuterated water (HDO), on the other hand, forms mostly on the dust grains in the cold clouds before core collapse (e.g., Jacq et al. 1990; Furuya et al. 2016). Particularly, the amount of HDO formed is set by a combination of the temperature and lifetime of the cold phase, where higher temperatures and shorter lifetimes lead to lower deuterium fractionation, and vice versa (e.g., Jensen et al. 2021). Once formed on the grains, HDO typically sublimates

into the gas phase near protostars, where the dust temperature exceeds 100 K, in so-called hot cores (high-mass stars) or hot corinos (low- and intermediate-mass stars; e.g., Herbst & van Dishoeck 2009). The amount of HDO present thus contains a fossil record of the conditions in the cold gas, and a key question naturally arises: how will different physical conditions in external galaxies affect these processes?

The first, and until now the only, extragalactic detection of HDO was reported by Muller et al. (2020). Using the Atacama Large Millimeter/submillimeter Array (ALMA), Muller et al. (2020) detected the HDO $J_{K_a,K_c} = 1_{01}-0_{00}$ absorption line at 464.9245 GHz in a spiral galaxy at a redshift (z) of 0.89 on the line of sight toward the quasar PKS 1830–211. Here, we report the first detection of HDO toward extragalactic hot molecular cores. Hot cores are compact ($\lesssim 0.1$ pc), warm ($\gtrsim 100$ K), and dense ($\gtrsim 10^{6-7} \text{ cm}^{-3}$) regions surrounding high-mass protostars very early in their evolution. A typical Galactic hot core is chemically rich, containing the products of the interstellar grain-surface chemistry (including complex organics and water) released from the dust grain ice mantles to the gas phase via thermal evaporation and/or sputtering in shock waves (e.g., Garay & Lizano 1999; Kurtz et al. 2000; Cesaroni 2005; Palau et al. 2011). Hot cores may also display



Original content from this work may be used under the terms of the [Creative Commons Attribution 4.0 licence](https://creativecommons.org/licenses/by/4.0/). Any further distribution of this work must maintain attribution to the author(s) and the title of the work, journal citation and DOI.

products of post-desorption gas chemistry (e.g., Herbst & van Dishoeck 2009; Oberg 2016; Jørgensen et al. 2020).

We detected the HDO $2_{11}-2_{12}$ line at 241.5616 GHz with ALMA toward hot cores N 105–2 A and N 105–2 B in the star-forming region N 105 in the Large Magellanic Cloud (LMC; briefly reported in Sewiło et al. 2022). These are two out of only a handful of known bona fide extragalactic hot cores, all located in the LMC (Shimonishi et al. 2016b, 2020; Sewiło et al. 2018, 2019, 2022).

The LMC, an irregular dwarf galaxy, is the most massive and one of the nearest (50.0 ± 1.1 kpc; Pietrzyński et al. 2013) satellites of the Milky Way. The low metallicity of the LMC ($Z \sim 0.3-0.5 Z_{\odot}$; Russell & Dopita 1992; Westerlund 1997; Rolleston et al. 2002), similar to galaxies at the peak of star formation in the Universe ($z \sim 1.5$; e.g., Pei et al. 1999; Mehrt et al. 2002; Madau & Dickinson 2014), provides a unique opportunity to study star formation (including the H₂O and HDO chemistry) in an environment that is significantly different than in today's Galaxy.

There are several factors that can directly impact the formation and destruction of H₂O and HDO molecules in a low-metallicity environment. The abundance of atomic O in the LMC is over a factor of two lower when compared with the Galaxy (i.e., fewer O atoms are available for water chemistry; e.g., Russell & Dopita 1992). The dust-to-gas ratio in the LMC is lower (e.g., Dufour 1975, 1984; Koornneef 1984; Roman-Duval et al. 2014), resulting in fewer dust grains for surface chemistry and less shielding than in the Galaxy. The deficiency of dust combined with the harsher UV radiation field in the LMC (e.g., Browning et al. 2003; Welty et al. 2006) leads to warmer dust temperatures (e.g., van Loon et al. 2010a) and consequently, less efficient grain-surface reactions (e.g., Shimonishi et al. 2016a; Acharyya & Herbst 2015). The cosmic-ray density in the LMC is about 25% of that measured in the solar neighborhood (e.g., Abdo et al. 2010; Knöldlseder 2013), resulting in less effective cosmic-ray-induced UV radiation.

Extragalactic deuterated molecules were first detected in star-forming regions of the LMC by Chin et al. (1996) in single-dish observations. Deuterated formyl cation (DCO⁺) was detected toward three (N 113, N 44 BC, N 159 HW) and deuterated hydrogen cyanide (DCN) toward one star-forming region (N 113; see also Wang et al. 2009). In an independent study, Heikkilä et al. (1997) reported a detection of DCO⁺ and a tentative detection of DCN toward N 159.

In the more recent interferometric studies, deuterated molecules have been detected toward the LMC hot cores and hot core candidates. DCN was detected in two hot cores in N 113 (N 113 A1 and N 113 B3; Sewiło et al. 2018), deuterated hydrogen sulfide (HDS) toward a hot core candidate N 105–2 C, HDO toward hot cores N 105–2 A and N 105–2 B, and deuterated formaldehyde (HDCO) toward N 105–2 A (Sewiło et al. 2022). In this paper, we provide a detailed discussion on the detection of HDO toward N 105–2 A and 2 B: the first detection of HDO toward an extragalactic hot core.

2. The Data

Field N 105–2 in the star-forming region LHA 120–N 105 (hereafter N 105; Henize 1956) hosting hot cores 2 A and 2 B was observed with ALMA 12 m Array in Band 6 as part of the Cycle 7 project 2019.1.01720.S (PI M. Sewiło; Sewiło et al. 2022). The observations were executed twice on 2019 October

21 with 43 antennas and baselines from 15 m to 783 m. The (bandpass, flux, phase) calibrators were (J0519–4546, J0519–4546, J0440–6952) and (J0538–4405, J0538–4405, J0511–6806) for the first and second run, respectively. N 105–2 was observed again on 2019 October 23 with 43 antennas, baselines from 15 m to 782 m, and the same calibrators. The total on-source integration was ~ 13.1 minutes. The spectral setup included four 1875 MHz spectral windows with 3840 channels centered on frequencies of 242.4 GHz, 244.8 GHz, 257.85 GHz, and 259.7 GHz; the spectral resolution is $1.21-1.13 \text{ km s}^{-1}$.

The data were calibrated and imaged with version 5.6.1-8 of the ALMA pipeline in CASA (Common Astronomy Software Applications; McMullin et al. 2007). Continuum was subtracted in the UV domain from the line spectral windows. The CASA task `tclean` was used for imaging using the Hogbom deconvolver, standard gridded, Briggs weighting with a robust parameter of 0.5, and auto-multithresh masking. The spectral cubes have a cell size of $0.^{\prime\prime}092 \times 0.^{\prime\prime}092 \times 0.56 \text{ km s}^{-1}$ and they have been corrected for primary beam attenuation.

Here, we present the results based on the 242.4 GHz spectral window: a detection of the HDO $2_{11}-2_{12}$ transition at 241,561.550 MHz with the upper energy level E_U of 95.2 K toward two continuum sources (A and B) in the N 105–2 field (see Figure 1). Sensitivity of 1.97 mJy per $0.^{\prime\prime}54 \times 0.^{\prime\prime}50$ beam (0.15 K) was achieved in the 242.4 GHz cube. Sensitivity of 0.05 mJy per $0.^{\prime\prime}51 \times 0.^{\prime\prime}47$ beam (4.4 mK) was achieved in the continuum.

3. Results

Figure 2 shows selected frequency ranges of the ALMA Band 6 spectra of hot cores N 105–2 A and B, covering the HDO 241.6 GHz line, as well as the methanol (CH₃OH) $J=5-4$ Q-branch at ~ 241.8 GHz and the methyl cyanide (CH₃CN) 14_K-13_K ladder for reference. The molecular line identification and spectral modeling for all spectral windows were performed for all the continuum sources in N 105–2 in Sewiło et al. (2022).

The spectral line modeling was performed using a least-squares approach under the assumption of local thermodynamic equilibrium (LTE) and accounting for line opacity effects. The best-fitting column density, rotational temperature, Doppler shift, and spectral line width ($[N^i, T_{\text{rot}}^i, v_i, dv^i]$) for the complete set of species were determined simultaneously. A custom Python routine was used to generate spectral line models with spectroscopic parameters taken from the Cologne Database for Molecular Spectroscopy (CDMS,¹⁴ Müller et al. 2001) for all molecular species except HDO (not included in CDMS) for which the data were taken from the Jet Propulsion Laboratory (JPL) Molecular Spectroscopy Database¹⁵ (Pickett et al. 1998). For molecular species with single line detections (including HDO), the rotational temperature of CH₃CN, $T_{\text{CH}_3\text{CN}}$, was adopted for the fitting. For N 105–2 A and 2 B, the HDO and CH₃CN integrated intensity peaks coincide, supporting this assumption (see Figures 1 and 5).

The Sewiło et al. (2022)'s LTE spectral-fitting results for HDO ($[N, v, dv] = [N_{\text{HDO}}, v_{\text{LSR}}, \Delta v_{\text{FWHM}}]$) and the adopted $T_{\text{CH}_3\text{CN}}$ are provided in Table 1 for N 105–2 A and 2 B. The synthetic spectra are overlaid on the observed spectra of

¹⁴ <http://www.astro.uni-koeln.de/cdms>

¹⁵ <http://spec.jpl.nasa.gov/>

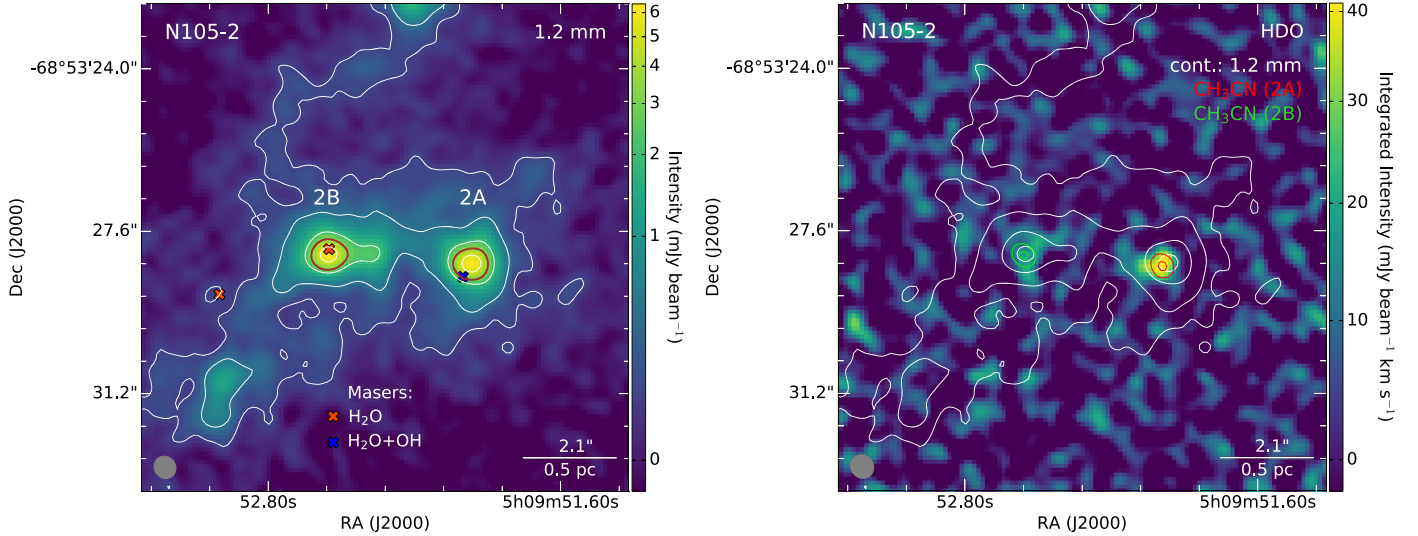


Figure 1. Left: the 1.2 mm continuum image of N 105–2 with spectral extraction regions for 2 A and 2 B indicated in brown; they are contours corresponding to 50% of the continuum peak of the corresponding source (6.4 and 6.2 mJy beam $^{-1}$ for 2 A and 2 B, respectively). Right: the HDO 2 $_{11}$ –2 $_{12}$ integrated intensity (moment 0) image of N 105–2 for a velocity range from 240.4 to 250.7 km s $^{-1}$. Red/green contours correspond to (50, 90)% of the CH $_3$ CN integrated intensity peak of 0.38/0.19 Jy beam $^{-1}$ km s $^{-1}$ for 2 A/2 B. White contours in both panels represent the 1.2 mm continuum emission with contour levels of (3, 10, 40, 100) \times the image rms noise level (σ) of 5.1×10^{-5} Jy beam $^{-1}$. The positions of H $_2$ O and OH masers are indicated in the left panel. The size of the synthesized beam is shown in the lower left corner of each image.

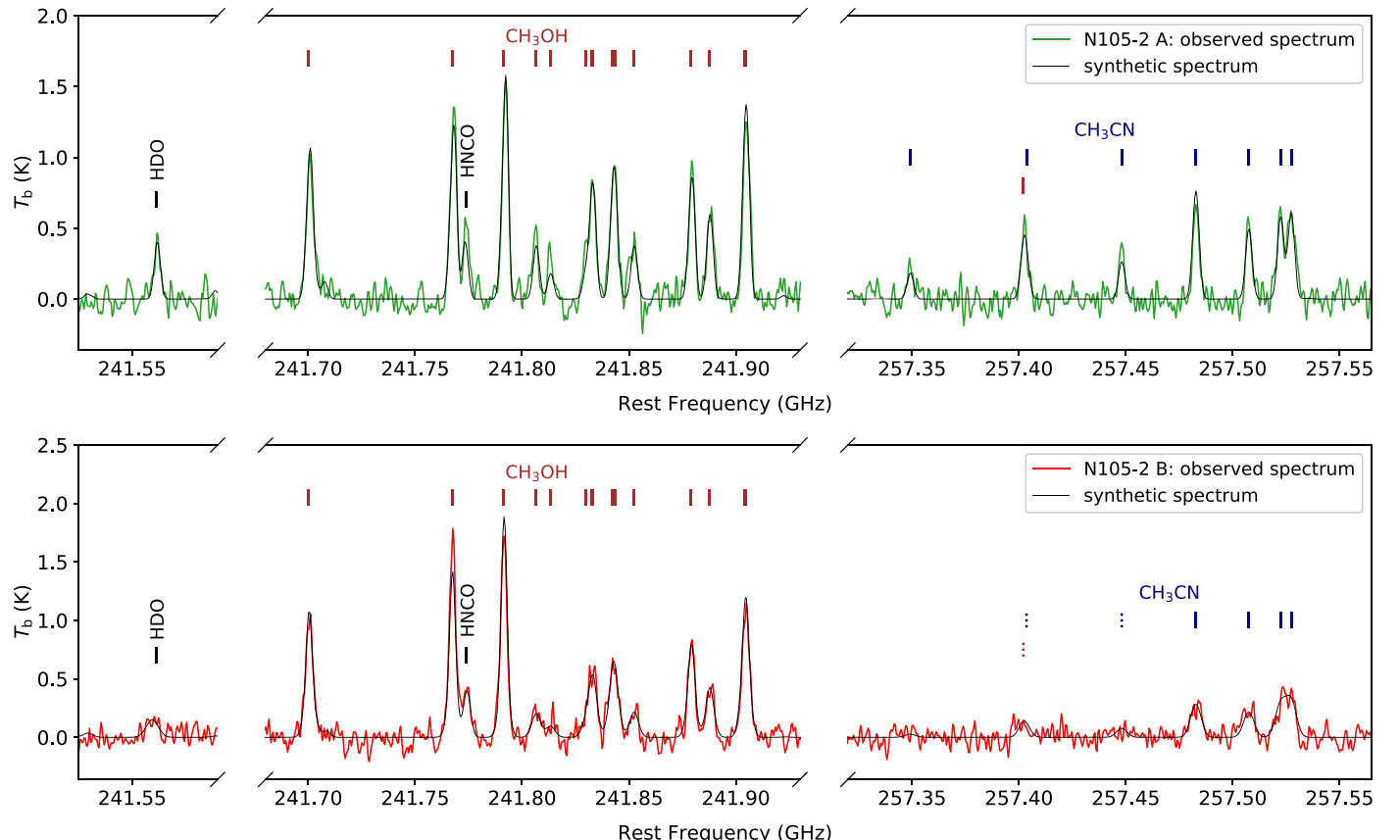


Figure 2. Selected frequency ranges of the ALMA Band 6 spectra of hot cores N 105–2 A (top) and 2 B (bottom), covering the HDO 2 $_{11}$ –2 $_{12}$ line, as well as the CH $_3$ OH $J = 5$ –4 Q-branch and the CH $_3$ CN 14 $_K$ –13 $_K$ ladder for reference. The tentatively detected transitions are indicated with dotted lines. The synthetic spectra from Sewilo et al. (2022) are shown in black.

2 A and 2 B in Figure 2. Table 1 also lists the H $_2$ column densities (N_{H_2}), H $_2$ number densities (n_{H_2}), and HDO abundances with respect to H $_2$ ($N_{\text{HDO}}/N_{\text{H}_2}$). N_{H_2} was calculated

by Sewilo et al. (2022) based on the 1.2 millimeter continuum flux density and adopting $T_{\text{CH}_3\text{CN}}$ under the assumption that the dust and gas are well coupled. The assumption of thermal

Table 1
A Summary of the Physical Properties of the LMC Hot Cores with the HDO Detection N 105–2 A and 2 B (Sewilo et al. 2022)

Parameter	N 105–2 A	N 105–2 B
$T_{\text{CH}_3\text{CN}}$ (K)	152_{-11}^{+10}	88_{-9}^{+10}
N_{HDO} (cm $^{-2}$)	$(4.9_{-0.4}^{+0.5}) \times 10^{14}$	$(2.6 \pm 0.5) \times 10^{14}$
v_{LSR} (km s $^{-1}$)	242.7 ± 0.2	$245.8_{-0.7}^{+0.8}$
Δv_{FWHM} (km s $^{-1}$)	4.2 ± 0.4	$8.2_{-1.8}^{+2.3}$
N_{H_2} (cm $^{-2}$)	$(1.8 \pm 0.2) \times 10^{23}$	$(3.1 \pm 0.5) \times 10^{23}$
n_{H_2} (cm $^{-3}$)	$\sim 4.6 \times 10^5$	$\sim 7.8 \times 10^5$
$N_{\text{HDO}}/N_{\text{H}_2}$	$(2.7 \pm 0.4) \times 10^{-9}$	$(8.2_{-2.0}^{+2.1}) \times 10^{-10}$

equilibrium between the dust and gas holds for high-density regions such as N 105–2 A and 2 B ($n_{\text{H}_2} \gtrsim 10^5$ cm $^{-3}$; e.g., Goldsmith & Langer 1978; Kaufman et al. 1998).

We have measured the HDO 2₁₁–2₁₂ line flux (the integrated line intensity; F_{HDO}) of 1.8 ± 0.3 K km s $^{-1}$ for N 105–2 A and 1.3 ± 0.6 K km s $^{-1}$ for 2 B. We have calculated the HDO 2₁₁–2₁₂ line luminosity (L_{HDO}) from F_{HDO} using the standard relation (e.g., Wu et al. 2005) as outlined in Appendix A. L_{HDO} is $(3.0 \pm 0.5) \times 10^{-2} L_{\odot}$ for 2 A and $(2.2 \pm 1.0) \times 10^{-2} L_{\odot}$ for 2 B. The results are listed in Table 2 in Appendix A.

3.1. The Galactic Sample of Hot Cores with the HDO Detection

HDO observations are available in the literature for 17 Galactic hot cores. The HDO 2₁₁–2₁₂ line fluxes (same transition we detected in the LMC) are available for W3(H₂O), AFGL 2591, G34.26+0.15, W51 e1/e2, W51 d, NGC 7538 IRS1, Sgr B2(N), and Sgr B2(M) near the Galactic Center, and the extreme outer Galaxy source WB 89–789 SMM1.

Observations of W3(H₂O) were performed with the James Clerk Maxwell Telescope (JCMT) with a 19'' beam (half-power beamwidth, HPBW), tracing 0.2 pc linear scales (Helmich et al. 1996). The HDO data for AFGL 2591 (van der Tak et al. 2006), G34.26+0.15 (Coutens et al. 2014), W51 e1/e2, W51 d, and NGC 7538 IRS1 (Jacq et al. 1990), were obtained with the IRAM 30 m telescope with a 12'' beam, tracing 0.15–0.32 pc scales for the distance range covered by these sources. The Sgr B2(N) and Sgr B2(M) observations were performed with the SEST telescope with a 22'' beam, tracing 0.89 pc scales (Nummela et al. 2000). WB 89–789 SMM1 was observed with ALMA by Shimonishi et al. (2021) with a $\sim 0.5''$ beam, corresponding to ~ 0.026 pc.

Two HDO transitions were detected toward W43 MM1, NGC 7538 S, IRAS 18089–1732 (Marseille et al. 2010), and W33A (van der Tak et al. 2006) with the IRAM 30 m telescope: 1₁₀–1₁₁ (80.5783 GHz, $E_{\text{U}} = 46.8$ K; 30'' beam, 0.34–0.80 pc scales) and 3₁₂–2₂₁ (225.8967 GHz, $E_{\text{U}} = 167.6$ K; 11'' beam, 0.12–0.31 pc scales). Assuming that these two transitions are optically thin and in LTE (see e.g., Persson et al. 2014), we have used a rotational diagram (Goldsmith & Langer 1999) to estimate the HDO 2₁₁–2₁₂ line flux toward W43 MM1, NGC 7538 S, IRAS 18089–1732, and W33A (see Appendix A).

Data for a single HDO transition, 3₁₂–2₂₁, are available for G9.62+0.19, G10.47+0.03A, G29.96–0.02, and G31.41+0.31 (Gensheimer et al. 1996); the IRAM 30 m telescope observations of these sources trace 0.2–0.6 pc scales. To estimate the HDO 2₁₁–2₁₂ line flux, we extrapolated the

3₁₂–2₂₁ line flux assuming an excitation temperature derived in literature for these sources using CH₃CN: 70 K for G9.62+0.19 (Hofner et al. 1996), 164 K for G10.47+0.03A (Olmi et al. 1996), 160 K for G29.96–0.02 (Beltrán et al. 2011), and 158 K for G31.41+0.31 (Beltrán et al. 2005). The calculated values of the HDO 2₁₁–2₁₂ line flux for G9.62+0.19, G10.47+0.03A, G29.96–0.02, and G31.41+0.31 are the most uncertain of all Galactic sources in our sample. However, in Appendix A, we show that the results for G9.62+0.19, G10.47+0.03A, G29.96–0.02, and G31.41+0.31 do not change significantly when different values of temperature are adopted (60–200 K).

We have derived the HDO 2₁₁–2₁₂ line luminosities from line fluxes for Galactic hot cores using the same formula as for N 105–2 A and 2 B. The value of L_{HDO} spans three orders of magnitude, ranging from $3.8 \times 10^{-3} L_{\odot}$ for WB 89–789 SMM1 to $8.2 L_{\odot}$ for Sgr B2(N). Both the HDO 2₁₁–2₁₂ line fluxes and luminosities for Galactic hot cores analyzed in this paper are provided in Table 2 in Appendix A.

Our ALMA observations of a star-forming region in the LMC at ~ 50 kpc with a resolution of $\sim 0.5''$ probe physical scales of 0.12–0.13 pc, similar to those traced by the observations of Galactic sources with single-dish telescopes such as the IRAM 30 m at 241.6 GHz, at a distance of ~ 2 kpc.

4. Discussion

4.1. HDO 2₁₁–2₁₂ Line Luminosity: LMC versus Galactic Hot Cores

Figure 3 shows the HDO 2₁₁–2₁₂ line luminosities (L_{HDO}) measured toward Galactic and LMC hot cores as a function of bolometric luminosity (L_{bol}). L_{bol} of Galactic hot cores ranges from $8.4 \times 10^3 L_{\odot}$ for WB 89–789 SMM1 to $1.2 \times 10^7 L_{\odot}$ for Sgr B2(M). The values of L_{bol} were adopted from Shimonishi et al. (2021) for WB 89–789 SMM1, Wright et al. (2012) for NGC 7538 S, Hofner et al. (1996) for G9.62+0.19, Ahmadi et al. (2018) for W3(H₂O), Hernández-Hernández et al. (2014) and van der Tak et al. (2013) for W51 e1/e2, Roloffs et al. (2011) for W51 d, Schmiedeke et al. (2016) for Sgr B2(N) and Sgr B2(M), and van der Tak et al. (2013) for the remaining sources.

There are uncertainties in L_{bol} related to a relatively low resolution of the single-dish observations. For example, the bolometric luminosities of G29.96–0.02 and G34.26+0.15 likely include contributions from both hot cores and nearby ultracompact (UC) H II regions. The HDO emission toward both regions was detected with the IRAM 30 m telescope and thus all of these components were within the half-power beamwidth. We do, however, expect most of the HDO emission to come from hot cores rather than more evolved UC H II regions.

Insufficient multiwavelength high-resolution data are available to determine individual L_{bol} for the LMC hot cores N 105–2 A and 2 B. To make an estimate of their L_{bol} , we determined a combined L_{bol} based on the data from 3.6 μm to 1.2 mm and inferred a contribution from each source as described in Appendix B. We estimate that both N 105–2 A and 2 B have L_{bol} of $\sim 10^5 L_{\odot}$. Since the sample of Galactic hot cores used for the analysis covers a wide range of the Galactocentric distances (thus metallicities; see below), we did not apply a correction to L_{HDO} measured toward the LMC hot

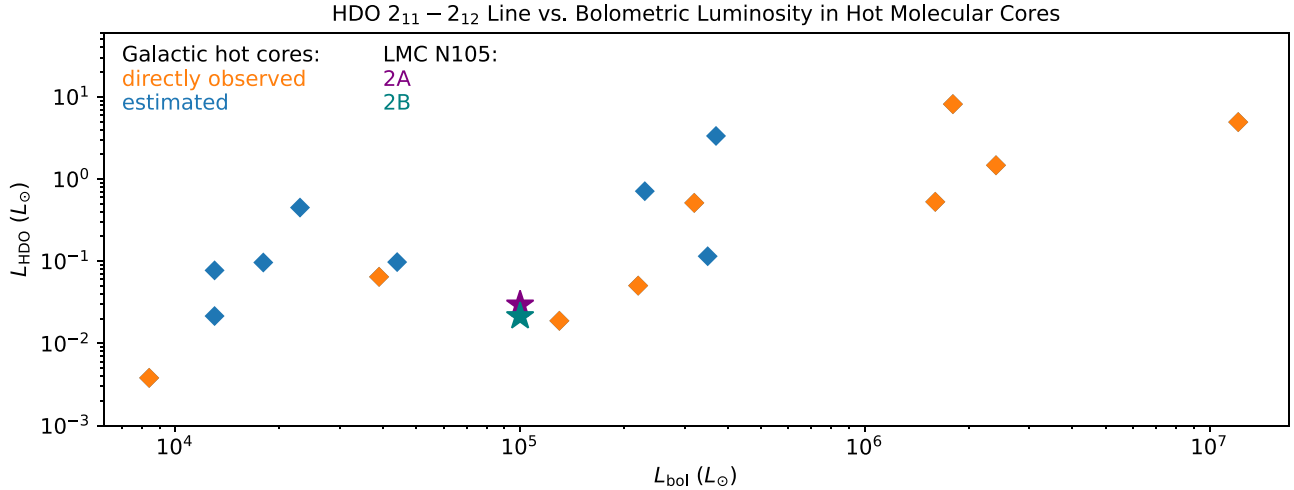


Figure 3. The HDO 241.6 GHz line luminosities (L_{HDO}) measured toward hot cores N 105–2 A and 2 B in the LMC and those observed toward a sample of hot cores in the Milky Way as a function of the bolometric luminosity (L_{bol}). The Galactic hot cores shown in the plot are (in order of increasing L_{bol}) WB 89–789 SMM1 (an extreme outer Galaxy source), NGC 7538 S and IRAS 18089–1732 ($L_{\text{HDO}} = 0.02 L_{\odot}$ and $0.08 L_{\odot}$, respectively), G9.62+0.19, W43 MM1, W3(H₂O), W33A, NGC 7538 IRS1, AFGL 2591, G31.41+0.31, G34.26+0.15, G29.96–0.02, G10.47+0.03A, W51 e1/e2, Sgr B2(N), W51d, and Sgr B2(M). The values of L_{HDO} indicated with orange diamonds are based on the observations of the HDO 2₁₁–2₁₂ transition, while those indicated with blue diamonds were estimated using the observations of other HDO transitions as described in Section 3.

cores to account for a difference in the metallicity between the LMC and the solar neighborhood.

The trend of increasing L_{HDO} with increasing L_{bol} for Galactic hot cores is very suggestive in Figure 3, especially when only the direct measurements of the HDO transition detected in the LMC are taken into account. The observed values of L_{HDO} for the LMC hot cores N 105–2 A and 2 B fit into this trend very well. The higher abundance of HDO for more luminous young stellar objects with hot cores is expected since the higher temperatures result in more HDO to be released from the icy grain mantles in hot core regions. L_{HDO} is also expected to scale with the total HDO column density which can be affected by low metallicity, a lower atomic O abundance in particular.

We can test the dependence of L_{HDO} on metallicity by investigating how L_{HDO} changes as a function of the Galactocentric distance (R_{GC}). The observations of a variety of objects including H II regions and Cepheid variable stars revealed radial elemental abundance gradients in the Milky Way disk (e.g., Churchwell & Walmsley 1975; Maciel & Andrievsky 2019 and references therein). Traced by O/H and Fe/H, metallicity decreases with increasing R_{GC} .

The O/H gradients based on Cepheids have slopes between -0.05 dex/kpc and -0.06 dex/kpc; similar slopes within the uncertainties have been obtained for the Fe/H gradients (e.g., Maciel & Andrievsky 2019 for over 300 Cepheids and $R_{\text{GC}} \sim 3$ –18 kpc). The O/H gradients from much smaller samples of H II regions are also similar to those measured from Cepheids within the uncertainties, ranging from -0.04 dex/kpc to -0.06 dex/kpc (e.g., Fernández-Martín et al. 2017 and references therein; Esteban & García-Rojas 2018).

We calculated R_{GC} for Galactic hot cores shown in Figure 3 based on their Galactic coordinates and distances (kinematic or parallax), and assuming the distance to the Galactic Center of 8.34 kpc (Reid et al. 2014). Located near the Galactic Center, Sgr B2(N) and Sgr B2(M) hot cores represent a high-metallicity environment ($Z_{\odot} < Z_{\text{GC}} \lesssim 2 Z_{\odot}$; Schultheis et al. 2019 and references therein) and have the highest L_{HDO} , while the extreme outer Galaxy source WB 89–789 SMM1 with the

lowest L_{HDO} is in the low-metallicity environment ($\sim 0.25 Z_{\odot}$). In general, with increasing R_{GC} and thus decreasing O/H ratio (metallicity), L_{HDO} decreases (see the top panel in Figure 4).

Four Galactic hot cores with L_{HDO} most similar to that measured toward N 105–2 A and 2 B (NGC 7538 S, NGC 7538 IRS1, W3(H₂O), and AFGL 2591) have the largest R_{GC} (the lowest O/H ratio) with the exception of the extreme outer Galaxy source, ranging from 8.4 kpc (AFGL 2591) to ~ 10 kpc (W3(H₂O)). AFGL 2591 is associated with the Local Arm, while the remaining sources with the Perseus arm (Reid et al. 2019). L_{HDO} for three out of four sources (NGC 7538 IRS1, W3(H₂O), and AFGL 2591) are based on the directly measured HDO 241.6 GHz transition. Based on studies on the radial elemental abundance gradients, the metallicity Z at 10 kpc ranges from $0.5 Z_{\odot}$ to $1.1 Z_{\odot}$ depending on the tracers used. Lower values of Z have been obtained from observations of H II regions (e.g., Rudolph et al. 2006; Esteban & García-Rojas 2018), while the higher values were obtained from Cepheids (e.g., Maciel & Andrievsky 2019; Luck & Lambert 2011). While the value of Z at a given R_{GC} is rather uncertain, it is clear that L_{HDO} of the LMC hot cores compares to L_{HDO} of objects located at larger R_{GC} where the oxygen abundance is lower and thus less oxygen is available for chemistry. In fact, the positions of the LMC hot cores N 105–2 A and 2 B fit in the trend seen in the top panel in Figure 3 very well for different O/H radial gradients determined in the H II region studies (see the Figure 3 caption for references), assuming the LMC's value of $12 + \log(\text{O/H})$ of 8.4 (e.g., Russell & Dopita 1992).

Decreasing L_{HDO} with increasing R_{GC} cannot be attributed solely to decreasing metallicity because L_{bol} shows a similar trend, as demonstrated in the middle panel in Figure 4. However, a weak metallicity dependence is still present in the $L_{\text{HDO}}/L_{\text{bol}}$ versus Z plot (i.e., with the L_{bol} dependence removed; see the lower panel in Figure 4). Even though L_{HDO} seems to be largely dependent on source luminosity, metallicity effects also play a role. Based on our data, we are not able to disentangle relative contributions of the bolometric

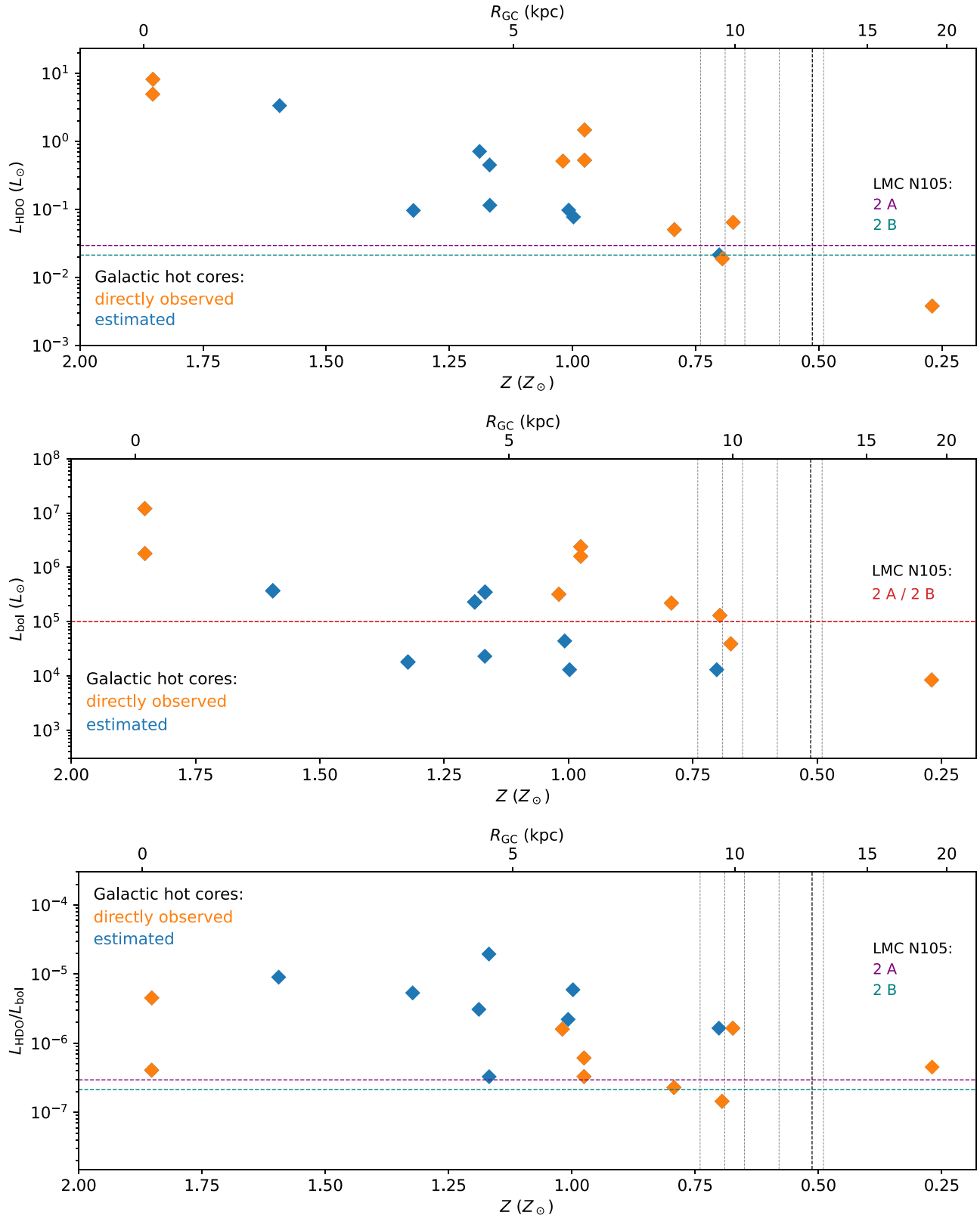


Figure 4. The HDO 241.6 GHz line luminosities (L_{HDO} ; upper panel), bolometric luminosities (L_{bol} ; middle panel), and the $L_{\text{HDO}}/L_{\text{bol}}$ ratio (lower panel) of the Galactic hot cores as a function of the Galactocentric distance (R_{GC}) and metallicity (Z). The metallicity at a given R_{GC} was calculated using Balser et al. (2011)’s O/H radial gradient $12 + \log(\text{O/H}) = -0.0446 R_{\text{GC}} + 8.962$ and adopting $[12 + \log(\text{O/H})]_{\odot}$ of 8.69 (Asplund et al. 2009): $\log(Z/Z_{\odot}) = \log(\text{O/H}) - \log(\text{O/H})_{\odot}$. The purple/teal solid lines in the upper panel indicate the measured L_{HDO} for the LMC hot cores N 105–2 A/2 B, while the red line in the lower panel corresponds to their roughly equal L_{bol} . The vertical black line indicates R_{GC} where $[12 + \log(\text{O/H})] = [12 + \log(\text{O/H})]_{\text{LMC}} = 8.4$ (e.g., Russell & Dopita 1992). The vertical gray lines indicate R_{GC} where $[12 + \log(\text{O/H})] = 8.4$ based on the O/H gradients found in other H II region studies, from left to right: Rudolph et al. (2006; far-IR data), Esteban & García-Rojas (2018), Arellano-Córdova et al. (2020), Fernández-Martín et al. (2017), and Rudolph et al. (2006; optical data). The orange and blue symbols are the same as in Figure 3.

luminosity (temperature) and metallicity (oxygen abundance) effects on L_{HDO} .

We did not find significant differences between Galactic hot cores and the LMC hot cores N 105–2 A and 2 B in terms of HDO; both L_{HDO} measured toward 2 A and 2 B fit in with the L_{HDO} versus L_{bol} and L_{HDO} versus Z trends observed toward Galactic hot cores.

4.2. H_2O in the LMC

4.2.1. Previous Studies on H_2O in the Magellanic YSOs

Water has previously been detected in the LMC in the solid phase (ice bands at $3.05\ \mu\text{m}$ and $62\ \mu\text{m}$; van Loon et al. 2005; Oliveira et al. 2006, 2011; Shimonishi et al. 2008, 2010, 2016a; van Loon et al. 2010b), gas phase (H_2O $2_{12}-1_{01}$ and $2_{21}-1_{10}$ transitions at $179.52\ \mu\text{m}$ and $108.07\ \mu\text{m}$; Oliveira et al. 2019), and as 22 GHz H_2O maser emission (interstellar H_2O masers in star-forming regions: Scalise & Braz 1981, 1982; Whiteoak et al. 1983; Whiteoak & Gardner 1986; van Loon & Zijlstra 2001; Lazendic et al. 2002; Oliveira et al. 2006; Ellingsen et al. 2010; Schwarz et al. 2012; Imai et al. 2013; circumstellar masers in evolved stars: van Loon et al. 1998, 2001; van Loon 2012).

The water ice studies demonstrated that ice abundances toward massive young stellar objects (YSOs) in the LMC are distinct from those observed toward Galactic YSOs. In particular, the $\text{CO}_2/\text{H}_2\text{O}$ column density ratio is two times higher in the LMC compared to the Galaxy (Gerakines et al. 1999; Seale et al. 2011), either due to an overabundance of CO_2 or underabundance of H_2O .

Oliveira et al. (2009) and Shimonishi et al. (2010) argue that the enhanced CO_2 production can be the result of the stronger radiation field and/or the higher dust temperature in the LMC; this scenario is supported by laboratory work (e.g., D'Hendecourt et al. 1986) and models of the diffusive grain-surface chemistry (e.g., Ruffle & Herbst 2001). Shimonishi et al. (2016a)'s "warm ice chemistry" model predicting that high dust temperatures in the LMC suppress the hydrogenation of CO on the grain surface, can reproduce both the enhanced abundance of CO_2 and underabundance of CH_3OH observed in the LMC.

However, based on a comparison of the H_2O , CO , and CO_2 ice column densities between the Galaxy, the LMC, and the Small Magellanic Cloud (SMC), Oliveira et al. (2011) concluded that high $\text{CO}_2/\text{H}_2\text{O}$ column density ratio combined with the relatively unchanged CO-to- CO_2 abundances are more consistent with the depletion of H_2O rather than an increased production of CO_2 . They attribute the depletion of H_2O to the combined effects of a lower dust-to-gas ratio and stronger UV radiation field in the LMC: the strong interstellar radiation penetrates deeper into the YSO envelopes as compared with Galactic YSOs, possibly destroying H_2O ice (enhancing photodesorption) in less-shielded outer layers, effectively reducing the observed H_2O ice column density. The CO_2 and H_2O ice mixtures that exist deeper in the envelope remain unaffected by the stronger radiation field.

Far-infrared spectroscopic observations toward massive YSOs in the LMC and SMC with Herschel/PACS revealed that H_2O and OH account for $\sim 10\%$ of the total line cooling, indicating that the trend of decreasing contribution of H_2O and OH cooling from low- to high-luminosity sources observed in

the Galaxy (Karska et al. 2014, 2018) extends to the massive LMC/SMC YSOs (Oliveira et al. 2019).

The abundance of 22 GHz H_2O masers in the LMC appears to be consistent with that observed in the Galaxy, making them useful signposts of massive star formation in the LMC in contrast to CH_3OH masers which are underabundant (e.g., Ellingsen et al. 2010).

4.2.2. Estimated H_2O Abundance in the LMC Hot Cores N 105–2 A and 2 B

Our observations did not cover any H_2O transitions, thus we cannot draw any reliable conclusions regarding the deuterium fractionation (the abundance ratio of deuterated over hydrogenated isotopologues, D/H) of water ($\text{HDO}/\text{H}_2\text{O}$) in the low-metallicity environment; however, since our data did not reveal differences between the Galactic and LMC hot cores N 105–2 A and 2 B based on the analysis of L_{HDO} , we made a rough estimate of the H_2O column densities and abundances toward 2 A and 2 B by assuming that $\text{HDO}/\text{H}_2\text{O}$ toward the LMC hot cores is the same as that observed in the Galaxy.

To date, the deuterium fractionation in the LMC was only determined for DCO^+ (for star-forming regions N 113, N 44 BC, and N 159 HW) and DCN (N 113) on $\sim 10\ \text{pc}$ scales (Chin et al. 1996; Heikkilä et al. 1997). The deuterium fractionation of DCO^+ ranges from 0.015 to 0.053, while the deuterium fractionation of DCN of 0.043 was found toward N 113. These values are similar to those observed toward Galactic dark clouds and pre-stellar cores: 0.01–0.1 (Ceccarelli et al. 2014 and references therein).

The typical values of water deuteration observed toward Galactic hot cores are of the order of $(2\text{--}8) \times 10^{-4}$, but they can be as high as $(2\text{--}5) \times 10^{-3}$ (van Dishoeck et al. 2021 and references therein). For example, $\text{HDO}/\text{H}_2\text{O} = (1.2, 0.8, 0.9, 1.6, 3.0) \times 10^{-3}$ for (G34.2+0.2, W51d, W51 e1/e2, Sgr B2(N), Orion KL) hot cores (Jacq et al. 1990; Neill et al. 2013).

We calculated the H_2O column densities for 2 A and 2 B for the maximum and minimum values in the Galactic $\text{HDO}/\text{H}_2\text{O}$ ranges provided above: 5×10^{-3} and 2×10^{-4} , using the HDO column densities for 2 A and 2 B provided in Section 3. For $\text{HDO}/\text{H}_2\text{O}$ of $(5 \times 10^{-3}, 2 \times 10^{-4})$, the H_2O column densities are $N(\text{H}_2\text{O}) \sim (9.8 \times 10^{16}, 2.5 \times 10^{18})\ \text{cm}^{-2}$ for 2 A and $(5.2 \times 10^{16}, 1.3 \times 10^{18})\ \text{cm}^{-2}$ for 2 B; the abundances with respect to H_2 are $X(\text{H}_2\text{O}) \sim (5.4 \times 10^{-7}, 1.4 \times 10^{-5})$ for 2 A and $(1.7 \times 10^{-7}, 4.2 \times 10^{-6})$ for 2 B.

The typical Galactic hot core H_2O abundances range from 5×10^{-6} to $> 10^{-4}$ (van Dishoeck et al. 2021), but a lower value of 1.7×10^{-6} was measured toward IRAS 16272–4837 by Herpin et al. (2016). The metallicity corrected (multiplied by a factor of two, $1/Z_{\text{LMC}}$; see Sewilo et al. 2022) values of $X(\text{H}_2\text{O})$ are $\sim (1.1 \times 10^{-6}, 2.8 \times 10^{-5})$ for 2 A and $\sim (3.4 \times 10^{-7}, 8.4 \times 10^{-6})$ for 2 B for the assumed $\text{HDO}/\text{H}_2\text{O}$ of $(5 \times 10^{-3}, 2 \times 10^{-4})$.

The $X(\text{H}_2\text{O})$ range for 2 A overlaps with the Galactic range for the most part, with the lower end about a factor of 2 lower than the minimum $X(\text{H}_2\text{O})$ measured in the Galactic hot cores. For 2 B, the $X(\text{H}_2\text{O})$ range is shifted toward lower values, down to $X(\text{H}_2\text{O})$ of about 5 times lower than the minimum $X(\text{H}_2\text{O})$ measured toward Galactic hot cores.

We have obtained a similar result for the analysis that only included sources closest in metallicity to that of the LMC and with measured deuterium fractionation of water; these are (W3(H_2O), AFGL 2591, NGC 7538 IRS1) with metallicities of

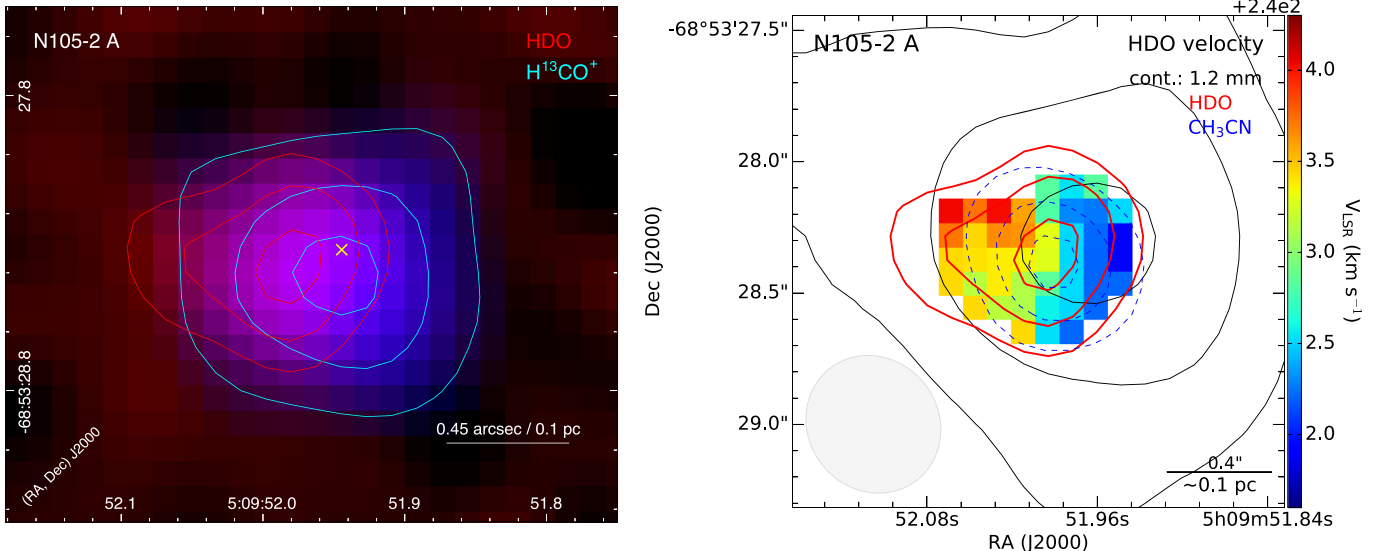


Figure 5. Left: two-color composite mosaic of N 105–2 A combining the integrated intensity images of HDO (red) and H^{13}CO^+ (blue). The red and cyan contours correspond to (30, 60, 90)% of the HDO and H^{13}CO^+ integrated intensity peak of 38.8 and $202.8 \text{ mJy beam}^{-1} \text{ km s}^{-1}$, respectively. The 1.2 mm continuum peak is indicated with an “x” symbol. Right: the HDO line velocity (moment 1) image of N 105–2 A. Red contours are the same as in the left panel. Dashed blue contours correspond to the CH_3CN emission with contour levels of (30, 60, 90)% of the CH_3CN integrated intensity peak of $378.6 \text{ Jy beam}^{-1} \text{ km s}^{-1}$. The 1.2 mm continuum emission contours are shown in black with contour levels of (10, 30, 90) σ .

$\sim(0.7, 0.8, 0.7) Z_\odot$ and HDO/ H_2O of $((2\text{--}6) \times 10^{-4}, 8 \times 10^{-4}, 3 \times 10^{-3})$. The HDO/ H_2O range for these three sources is basically the same as for the entire population of Galactic disk hot cores. If we adopt a higher end of the HDO/ H_2O range of 3×10^{-3} instead of 5×10^{-3} (as above) and scale the estimated LMC value to the average metallicity of W3(H_2O), AFGL 2591, NGC 7538 IRS1, the lower end of the $X(\text{H}_2\text{O})$ range for 2 A and 2 B is 20% higher, but our conclusions remain the same.

4.3. HDO Emission in N 105–2 A: the Spatial Distribution and Velocity Structure

The spatial distribution and velocity structure of the HDO emission in N 105–2 A is consistent with HDO being the product of the low-temperature dust grain chemistry.

In hot cores where the temperatures increase above 100 K, H_2O (and HDO) sublimates and becomes an effective destroyer of HCO^+ (e.g., van Dishoeck et al. 2021 and references therein). This scenario is confirmed in Galactic hot cores where an anticorrelation between H_2^{18}O (or CH_3OH which is a good proxy for the distribution of water as it desorbs at similar temperature) and H^{13}CO^+ has been observed (e.g., Jørgensen et al. 2013). We have compared the spatial distribution of HDO and H^{13}CO^+ toward 2 A and found that HDO and H^{13}CO^+ integrated intensity peaks are separated by $\sim 0.^{\prime\prime}19$ ($\sim 0.046 \text{ pc}$ or $\sim 9500 \text{ au}$ at 50 kpc; see Figure 5), while the peak of the CH_3OH emission is coincident with the HDO emission peak.

In addition to the positional anticorrelation between H_2O and HCO^+ , the anticorrelation in velocity is also expected (e.g., van Dishoeck et al. 2021). For N 105–2 A, the (HDO, H^{13}CO^+) velocities are $(242.7 \pm 0.2, 241.90 \pm 0.02) \text{ km s}^{-1}$ (Sewilo et al. 2022), so there is a small velocity difference of $0.8 \pm 0.2 \text{ km s}^{-1}$ between HDO and H^{13}CO^+ . The anticorrelation in both the position and velocity between HDO and H^{13}CO^+ toward 2 A is consistent with the observations of Galactic hot cores and supports the dust-grain chemistry origin of HDO in 2 A.

The HDO velocity distribution in 2 A is inconsistent with the shock origin of the HDO emission. We detected an HDO velocity gradient of $\sim 12 \text{ km s}^{-1} \text{ pc}^{-1}$ that could indicate the presence of an outflow and HDO production in an outflow-driven shock (see Figure 5); however, the HDO line is relatively narrow ($4.2 \pm 0.4 \text{ km s}^{-1}$, $\sim 1 \text{ km s}^{-1}$ broader than the H^{13}CO^+ line), making this scenario unlikely. The velocity gradient likely traces the rotation of the core.

Note that we have not performed the similar analysis for 2 B because the HDO emission toward this source is much fainter and the results are inconclusive.

5. Conclusions

Based on the analysis of the HDO emission detected toward hot cores N 105–2 A and 2 B in the LMC and a sample of Galactic hot cores covering a range of bolometric luminosities and Galactocentric distances (metallicities), we have found that L_{HDO} measured toward these LMC hot cores follow both the bolometric luminosity and metallicity dependence traced by Galactic sources. Based on our data, we are not able to disentangle the effects of the bolometric luminosity (temperature) and metallicity (oxygen abundance) on L_{HDO} , but our results indicate that L_{bol} likely has a larger impact on L_{HDO} than does metallicity.

We have found that if the water deuterium fractionation in the LMC hot cores N 105–2 A and 2 B is within the range observed in the Galactic hot cores, the range of the estimated H_2O abundances toward 2 A and 2 B is shifted toward lower than Galactic values.

The spatial distribution and velocity structure of the HDO emission in N 105–2 A is consistent with HDO being the product of the low-temperature dust grain chemistry.

The astrochemical models of deuterated species predict that HDO is abundant regardless of the extragalactic environment (starburst, cosmic-ray-enhanced environments, low metallicity, and high-redshift galaxies) and should be detectable with ALMA in many diverse galaxies (Bayet et al. 2010). Our results

for the LMC and the detection of HDO toward the $z = 0.89$ absorber against the quasar PKS 1830–211 by Muller et al. (2020) are in agreement with these model predictions. Furthermore, our work demonstrates the utility of HDO as a tracer of H₂O chemistry, which is more readily accessible than H₂O using ground-based, millimeter-wave observations.

We thank the anonymous referee for comments that helped us improve the manuscript. The material is based upon work supported by NASA under award number 80GSFC21M0002 (M.S.). A.K. acknowledges support from the First TEAM grant of the Foundation for Polish Science No. POIR.04.04.00-00-5D21/18-00. This article has been supported by the Polish National Agency for Academic Exchange under grant No. PPI/APM/2018/1/00036/U/001. S.B.C., M.A.C., and E.G.B. were supported by the NASA Planetary Science Division Internal Scientist Funding Program through the Fundamental Laboratory Research work package (FLaRe). This research is supported by NSF award 2009624 to U Virginia (R. I.). The National Radio Astronomy Observatory is a facility of the National Science Foundation operated under cooperative agreement by Associated Universities, Inc. This paper makes use of the following ALMA data: ADS/JAO.ALMA#2019.1.01720.S. ALMA is a partnership of ESO (representing its member states), NSF (USA), and NINS (Japan), together with NRC (Canada), NSC and ASIAA (Taiwan), and KASI (Republic of Korea), in cooperation with the Republic of Chile. The Joint ALMA Observatory is operated by ESO, AUI/NRAO, and NAOJ. This research made use of APLpy, an open-source plotting package for Python (Robitaille & Bressert 2012).

Appendix A

Determination of the HDO Line Luminosity: Data and Methods

In Table 2, we have compiled the data used for our analysis of the LMC and Milky Way hot cores, both the quantities derived in this paper and the data from literature. The HDO $2_{11}-2_{12}$ line flux ($F_{\text{HDO } 2_{11}-2_{12}}$) forms the basis of the analysis, with 11 out of 19 values being directly measured. $F_{\text{HDO } 2_{11}-2_{12}}$ for the remaining sources was estimated from the observations of one or two other HDO transitions as described in Section 3. We have used $F_{\text{HDO } 2_{11}-2_{12}}$ to determine the HDO $2_{11}-2_{12}$ line luminosity ($L_{\text{HDO } 2_{11}-2_{12}}$).

The spectral line luminosity (L) can be derived based on the line flux (the integrated line intensity) using the standard relation that assumes a Gaussian beam and the Gaussian brightness distribution for the source (e.g., Wu et al. 2005, their

Equation (2)):

$$L = 23.5 \times 10^{-6} D^2 \frac{\pi \theta_s^2}{4 \ln 2} \frac{\theta_s^2 + \theta_{\text{beam}}^2}{\theta_s^2} \int T dv, \quad (\text{A1})$$

where D is the distance in kpc, θ_s and θ_{beam} are the angular sizes in arcseconds of the source and beam, respectively, and $\int T dv$ is the line flux in K km s⁻¹. We calculated $L_{\text{HDO } 2_{11}-2_{12}}$ from $\int T dv = F_{\text{HDO } 2_{11}-2_{12}}$, assuming a point source emission and adopting heliocentric distances from the literature.

In addition to the HDO $2_{11}-2_{12}$ line fluxes and luminosities, as well as the equatorial and Galactic coordinates, Table 2 also lists bolometric luminosities (L_{bol}), distances (D), and Galactocentric radii (R_{GC}). All references are provided in the table.

Below, we provide additional information on the analysis of the HDO $1_{10}-1_{11}$ and $3_{12}-2_{21}$ data for sources with no observed HDO $2_{11}-2_{12}$ transition.

IRAS 18089–1732, W43 MM1, W33A, NGC 7538 S: We used the HDO $1_{10}-1_{11}$ and $3_{12}-2_{21}$ data available for these sources to construct the rotational diagram and estimate the HDO $2_{11}-2_{12}$ line flux (see Section 3.1). The rotational diagram analysis provided us with the estimate of the HDO rotational temperature (T_{rot}) and column density (N_{HDO}): $T_{\text{rot}} = (82, 78, 110, 90)$ K and $N_{\text{HDO}} = (5.1, 5.0, 6.9, 1.0) \times 10^{14}$ cm⁻² for (IRAS 18089–1732, W43 MM1, W33A, and NGC 7538 S). Since the analysis was based only on two data points (two HDO transitions), we expect the uncertainties to be at least $\sim 50\%$. Our result for W33A is fully consistent with van der Tak et al. (2006) who analyzed the same HDO data.

G9.62+0.19, G10.47+0.03A, G29.96–0.02, G31.41+0.31: HDO $3_{12}-2_{21}$ is the only HDO transition available for these sources. As discussed in Section 3.1, to estimate the HDO $2_{11}-2_{12}$ line flux, we extrapolated the $3_{12}-2_{21}$ line flux in the rotational diagram assuming T_{rot} derived in the literature based on CH₃CN (Hofner et al. 1996; Olmi et al. 1996; Beltrán et al. 2005, 2011): (70, 164, 160, 158) K for (G9.62+0.19, G10.47+0.03A, G29.96–0.02, and G31.41+0.31). To investigate how adopting a different value of T_{rot} changes $L_{\text{HDO } 2_{11}-2_{12}}$, we have calculated it for all four sources assuming T_{rot} of 60, 100, and 200 K. The results are shown in Figures A1 and A2.

In Figures A1 and A2, we show the same L_{HDO} plots as in Figures 3 and 4, respectively, with additional data points (L_{HDO} determined for three different values of T_{rot}) overlaid. The figures show that the results for G9.62+0.19, G10.47+0.03A, G29.96–0.02, and G31.41+0.31 do not change significantly when different values of temperature are adopted and the conclusions of our work hold.

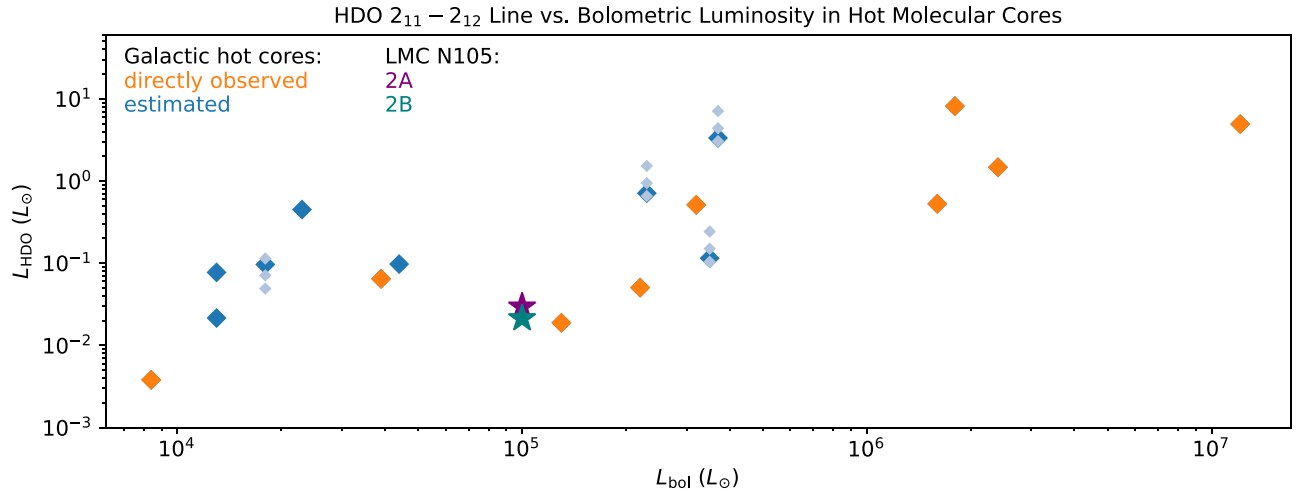


Figure A1. The same as in Figure 3 with additional data points shown in light blue for G9.62+0.19 ($L_{\text{bol}} = 1.8 \times 10^4 L_{\odot}$), G31.41+0.31 ($2.3 \times 10^5 L_{\odot}$), G29.96–0.02 ($3.5 \times 10^5 L_{\odot}$), and G10.47+0.03A ($3.7 \times 10^5 L_{\odot}$), demonstrating how L_{HDO} for these sources would change if different values of T_{rot} were adopted in the rotational diagram analysis (see Section 3.1). The data points correspond to T_{rot} of (from top to bottom): 60, 100, and 200 K. T_{rot} adopted from literature for (G9.62+0.19, G31.41+0.31, G29.96–0.02, G10.47+0.03A) is (70, 158, 160, 164) K. Adopting a different value of T_{rot} does not affect the overall L_{HDO} trend with L_{bol} for the Galactic sample of hot cores.

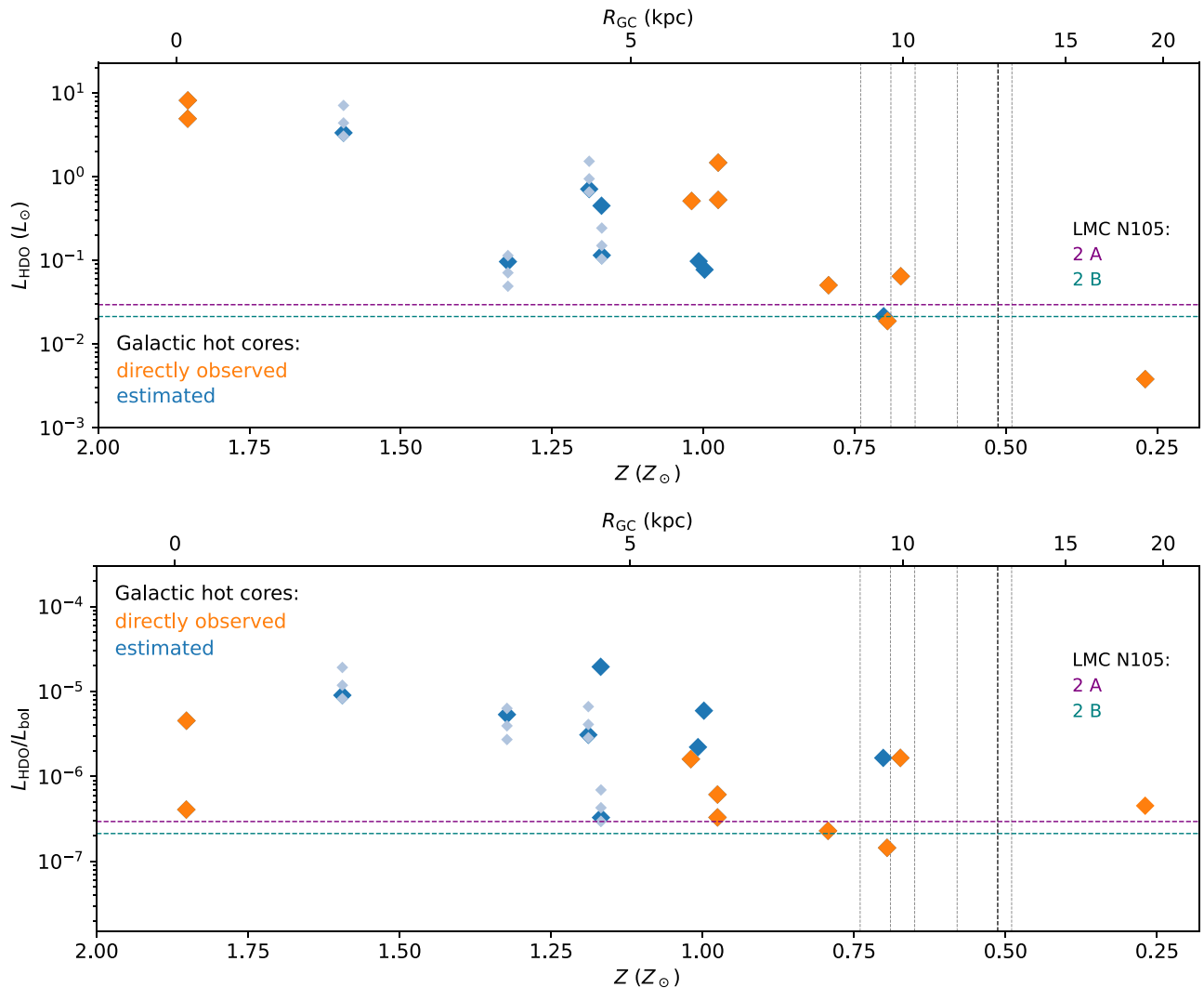


Figure A2. The same as in the top and bottom panel in Figure 4 with light blue diamonds as in Figure A1 for G10.47+0.03A ($Z \sim 1.6 Z_{\odot}$), G9.62+0.19 ($\sim 1.3 Z_{\odot}$), G31.41+0.31 ($\sim 1.2 Z_{\odot}$), and G29.96–0.02 ($\sim 1.2 Z_{\odot}$).

Table 2
A Compilation of the Data for the LMC N 105–2 A and 2 B Hot Cores and a Sample of Galactic Hot Cores used in the Analysis

Hot Core	R.A. ($^{\text{h}} \text{ m } \text{s}$)	Decl. ($^{\circ} \text{ ' } \text{"}$)	$F_{\text{HDO } 2_{11}-2_{12}}$ (K km s^{-1})	F_{HDO} Flag ^a	F_{HDO} Ref.	$L_{\text{HDO } 2_{11}-2_{12}}$ ($10^{-2} L_{\odot}$)	L_{bol} (L_{\odot})	L_{bol} Ref.	D (kpc)	D Ref.	l (deg)	b (deg)	R_{GC} (kpc)
LMC													
N 105–2 A	05:09:51.96	−68:53:28.3	1.8(0.3)	1	this paper	3.0(0.5)	$\sim 1.0 \times 10^5$	this paper	50	16	279.7526	−34.2520	...
N 105–2 B	05:09:52.56	−68:53:28.1	1.3(0.6)	1	this paper	2.2(1.0)	$\sim 1.0 \times 10^5$	this paper	50	16	279.7523	−34.2511	...
Milky Way													
IRAS 18089–1732	18:11:51.5	−17:31:29	1.24	2	1	7.73	1.3×10^4	9	2.3	17	12.8887	0.4897	6.12
NGC 7538 S	23:13:44.5	+61:26:50	0.23	2	1	2.15	1.3×10^4	10	2.8	18	111.533	0.7568	9.55
G9.62+0.19	18:06:15.0	−20:31:42	0.31	3	2	9.64	1.8×10^4	11	5.15	19	9.62	0.19	3.37
W43 MM1	18:47:47.0	−01:54:28	1.26	2	1	44.94	2.3×10^4	9	5.5	20	30.8175	−0.0571	4.58
W3(H ₂ O)	02:27:03.9	+61:52:25	1.2	1	3	6.45	3.9×10^4	12	2.14	21	133.9487	1.0649	9.95
W33A	18:14:39.1	−17:52:07	1.44	2	4	9.75	4.4×10^4	9	2.4	22	12.9069	−0.2589	6.02
NGC 7538 IRS1	23:13:45.3	+61:28:10	0.7(0.4)	1	5	1.88(1.08)	1.3×10^5	9	2.65	23	111.5422	0.7772	9.63
AFGL 2591	20:29:24.7	+40:11:19	0.394(0.080)	1	4	5.04(1.02)	2.2×10^5	9	3.3	24	78.8872	0.7085	8.36
G31.41+0.31	18:47:34.3	−01:12:46	0.97	3	2	71.1	2.3×10^5	9	7.9	25	31.41	0.31	4.42
G34.26+0.15	18:53:18.6	+01:14:58	12.27(0.05)	1	6	51.2(0.2)	3.2×10^5	9	3.3	26	34.26	0.15	5.91
G29.96−0.02	18:46:03.8	−02:39:22	0.35	3	2	11.49	3.5×10^5	9	5.3	27	29.96	−0.02	4.56
11 G10.47+0.03A	18:08:38.2	−19:51:50	3.89	3	2	334.35	3.7×10^5	9	8.55	19	10.47	0.03	1.56
W51 e1/e2	19:23:43.9	+14:30:29	4.7(1.1)	1	5	52.8(12.3)	1.6×10^6	9; 13	5.41	28	49.49	−0.39	6.34
Sgr B2(N)	17:46:07.9	+28:20:12	9.1	1	7	815.74	1.8×10^6	14	8.34	29	0.6773	−0.029	0.099
W51 d	19:23:39.6	+14:31:07	13.1(11.0)	1	5	147.0(123.5)	2.4×10^6	15	5.41	28	49.4904	−0.3695	6.34
Sgr B2(M)	17:46:08.2	+28:20:58	5.5	1	7	493.03	1.2×10^7	14	8.34	29	0.6672	−0.0364	0.097
WB89–789 SMM1	06:17:24.07	+14:54:42.3	5.05(0.29)	1	8	0.38(0.02)	8.4×10^3	8	10.7	30	195.8219	−0.568	18.86

Notes. (1) Marseille et al. 2010; (2) Gensheimer et al. 1996; (3) Helmich et al. 1996; (4) van der Tak et al. 2006; (5) Jacq et al. 1990; (6) Coutens et al. 2014; (7) Nummelin et al. 2000; (8) Shimonishi et al. 2021; (9) van der Tak et al. 2013; (10) Wright et al. 2012; (11) Hofner et al. 1996; (12) Ahmadi et al. 2018; (13) Hernández-Hernández et al. 2014; (14) Schmiedeke et al. 2016; (15) Roloffs et al. 2011; (16) Pietrzyński et al. 2013; (17) Xu et al. 2011; (18) Sandell et al. 2003; (19) Sanna et al. 2014; (20) Nguyen Luong et al. 2011; (21) Navareta et al. 2019; (22) Immer et al. 2013; (23) Moscadelli et al. 2008; (24) Rygl et al. 2012; (25) Churchwell et al. 1990; (26) Kuchar & Bania 1994; (27) Zhang et al. 2014; (28) Sato et al. 2010; (29) Reid et al. 2014; (30) Brand & Wouterloot 2007.

^a “ F_{HDO} flag” indicates whether the HDO $2_{11}-2_{12}$ line flux ($F_{\text{HDO } 2_{11}-2_{12}}$) is directly measured from the HDO $2_{11}-2_{12}$ line observations or estimated based on the observations of other HDO transitions: 1, the observed value; the uncertainties are provided when available; 2, estimated using the HDO $1_{10}-1_{11}$ and $3_{12}-2_{21}$ lines and the rotational diagram; the uncertainties are about 30%; 3, estimated using the HDO $3_{12}-2_{21}$ line and the rotational diagram, adopting the value of temperature from literature. See Section 3.1 for details.

^b $L_{\text{HDO } 2_{11}-2_{12}}$ is the HDO $2_{11}-2_{12}$ line luminosity calculated using Equation (A1).

^c R_{GC} is a Galactocentric distance calculated for Galactic hot cores based on their Galactic coordinates (l, b) and heliocentric distances (D ; kinematic or parallax), and assuming the distance to the Galactic Center of 8.34 kpc (Reid et al. 2014).

Appendix B

Bolometric Luminosity of N 105–2 A and 2 B

The multiwavelength data with high enough spatial resolution to resolve sources N 105–2 A and 2 B are not available at this time, thus we are not able to determine their individual bolometric luminosities (L_{bol}) independently. Instead, we have estimated their combined L_{bol} and inferred their individual contributions based on the highest resolution data.

To construct the multiwavelength spectral energy distribution (SED) of the combined sources N 105–2 A and 2 B (N 105–2 A/2 B), we have used the seven-band Spitzer Space Telescope photometric measurements from Gruendl & Chu (2009) covering 3.6–24 μm (catalog source 050952.26–685327.3; point-spread function's FWHMs $\sim 1.7\text{--}18''$; SAGE Team 2006), five-band Herschel Space Observatory photometric measurements from Seale et al. (2014) covering 100–500 μm (HSOBMHERICC J77.466495-68.891241; FWHMs $\sim 8.6\text{--}40.5''$; HERITAGE Team 2013), and a combined ALMA 1.2 mm continuum flux density from Sewilo et al. (2022). The 1.2 mm flux density has been calculated from the same area used by Gruendl & Chu (2009) to extract the Spitzer photometry. N 105–2 A and 2 B have no counterparts in the near-infrared catalogs such as 2MASS (Skrutskie et al. 2006; see also Gruendl & Chu 2009) or VISTA VMC (Cioni et al. 2011).

In addition, we have used the Spitzer InfraRed Spectrograph (IRS) spectrum from Seale et al. (2009) to better constrain the SED between 5.2 and 37.9 μm . We extracted 11 data points from the IRS spectrum that were selected at wavelengths free of fine-structure emission lines to delineate silicate features and the underlying continuum. The IRS data points at 20–30 μm have fluxes $\sim 50\%$ lower than the MIPS 24 μm catalog measurement and are likely due to the scaling factors that were applied additionally to match smoothly the spectrum segments taken under different modules across the full wavelength range (Seale et al. 2009). We have thus reverted these IRS fluxes to their original values for three affected spectrum segments by removing the corresponding scaling factors, i.e., dividing the fluxes within SL1 (short wavelength, low resolution; 7.6–14.6 μm), SH (short wavelength, high resolution; 9.9–19.3 μm), and LH (long wavelength, high resolution; 18.9–36.9 μm) modules by 1.091, 0.746, and 0.612, respectively. The resultant IRS fluxes are in good agreement with the MIPS 24 μm photometric flux measurement from Gruendl & Chu (2009).

The 70 μm photometry for 050952.26–685327.3 is not available in the existing catalogs (SAGE, Meixner et al. 2006; Gruendl & Chu 2009), therefore we performed an aperture photometry on the SAGE 70 μm image to estimate the 70 μm flux of N 105–2 A/2 B. We used an aperture with a 16'' radius, a 39''–65'' background annulus, and we applied an aperture correction factor of 2.087 (see also Chen et al. 2010).

The SED for N 105–2 A/2 B and multiwavelength image cutouts are shown in Figures B1 and B2, respectively.

While 2 A and 2 B were extracted as a single Spitzer source by Gruendl & Chu (2009), they are marginally resolved in all

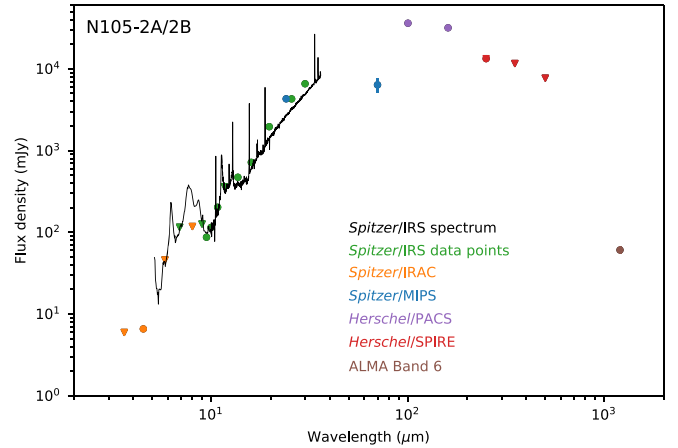


Figure B1. The spectral energy distribution (SED) for the combined sources N 105–2 A and 2 B, covering the wavelength range from 3.6 μm to 1.2 mm. Filled circles and triangles are valid flux values and flux upper limits, respectively. The flux error bars are plotted if larger than the data points.

Spitzer/IRAC images (see Figure B2). To assess individual flux contributions from N 105–2 A and 2 B to the combined, unresolved photometric measurements, we carried out aperture photometry of their counterparts on Spitzer/IRAC images. As the $\sim 2''$ separation between these two sources translates to ~ 1.5 pixels at IRAC's pixel scale, we used a 1-pixel radius to estimate their flux ratios. The 2 A to 2 B flux ratios are $\sim 1.4\text{--}1.6$ at 3.6 and 4.5 μm and ~ 1 at 5.8 and 8.0 μm . Comparable fluxes at longer Spitzer wavelengths (5.8 and 8.0 μm) and the small difference at shorter wavelengths (3.6 and 4.5 μm) suggest that the two sources are likely to contribute similarly to the unresolved measurements at longer wavelengths. In addition, 2 A and 2 B have the same continuum flux densities at 1.2 mm within the uncertainties. We thus assumed the unresolved fluxes are partitioned equally between 2 A and 2 B.

We have estimated L_{bol} in two ways. First, we fitted the SED of N 105–2 A/2 B with a set of radiative transfer model SEDs for YSOs developed by Robitaille (2017) using the Robitaille et al. (2007) SED fitting tool. We selected the best-fit model using the procedure outlined in Sewilo et al. (2019); it includes both an envelope and a disk, consistent with the classification of 2 A and 2 B as hot cores. Considering the fact that the SED corresponds to two objects, we only use the fitting results to determine luminosity. The 70 μm flux has a large uncertainty that can only be improved with higher-resolution observations. It is difficult to judge whether the 70 μm flux is a lower or an upper limit (see Figure B2) and hence the data point carries little weight in the fitting. We have obtained L_{bol} of $\sim 10^5 L_{\odot}$ for each N 105–2 A and N 105–2 B.

To estimate L_{bol} , we also used the trapezoidal method to sum up the area under the SED resulting in L_{bol} of $2.4 \times 10^5 L_{\odot}$, consistent with the SED fitting results. In this method, we excluded the 70 μm flux and treated all the remaining fluxes as valid data points.

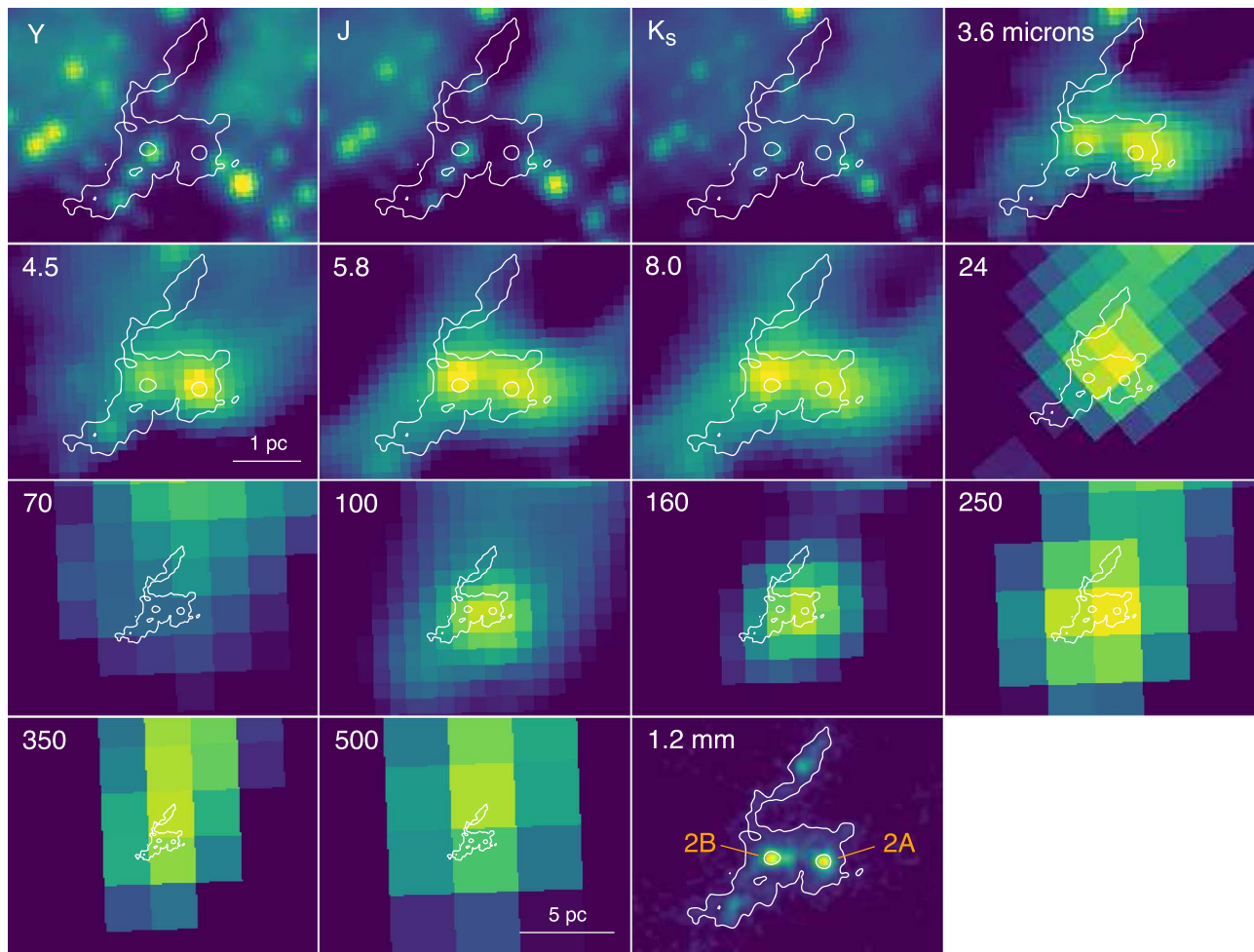


Figure B2. Multiwavelength images of N 105-2 A and 2 B (from left to right, top to bottom): VISTA VMC YJK_s (Cioni et al. 2011), Spitzer/SAGE IRAC 3.6–8.0 μm , and MIPS 24 and 70 μm (Meixner et al. 2006; SAGE Team 2006), Herschel/HERITAGE PACS 100 and 160 and SPIRE 250–500 μm (Meixner et al. 2013; HERITAGE Team 2013), and ALMA 1.2 mm (Sewilo et al. 2022). The 1.2 mm continuum contours with contour levels of (3, 50) times the image rms of $5.1 \times 10^{-5} \text{ mJy beam}^{-1}$ are overlaid on all the images for reference.

ORCID iDs

Marta Sewilo [ID](https://orcid.org/0000-0003-2248-6032) <https://orcid.org/0000-0003-2248-6032>
 Agata Karska [ID](https://orcid.org/0000-0001-8913-925X) <https://orcid.org/0000-0001-8913-925X>
 Lars E. Kristensen [ID](https://orcid.org/0000-0003-1159-3721) <https://orcid.org/0000-0003-1159-3721>
 Steven B. Charnley [ID](https://orcid.org/0000-0001-6752-5109) <https://orcid.org/0000-0001-6752-5109>
 C.-H. Rosie Chen [ID](https://orcid.org/0000-0002-3925-9365) <https://orcid.org/0000-0002-3925-9365>
 Joana M. Oliveira [ID](https://orcid.org/0000-0002-0861-7094) <https://orcid.org/0000-0002-0861-7094>
 Martin Cordiner [ID](https://orcid.org/0000-0001-8233-2436) <https://orcid.org/0000-0001-8233-2436>
 Jennifer Wiseman [ID](https://orcid.org/0000-0002-1143-6710) <https://orcid.org/0000-0002-1143-6710>
 Álvaro Sánchez-Monge [ID](https://orcid.org/0000-0002-3078-9482) <https://orcid.org/0000-0002-3078-9482>
 Jacco Th. van Loon [ID](https://orcid.org/0000-0002-1272-3017) <https://orcid.org/0000-0002-1272-3017>
 Remy Indebetouw [ID](https://orcid.org/0000-0002-4663-6827) <https://orcid.org/0000-0002-4663-6827>
 Peter Schilke [ID](https://orcid.org/0000-0003-2141-5689) <https://orcid.org/0000-0003-2141-5689>
 Emmanuel Garcia-Berrios [ID](https://orcid.org/0000-0002-1069-2931) <https://orcid.org/0000-0002-1069-2931>

References

Abdo, A. A., Ackermann, M., Ajello, M., et al. 2010, [A&A](#), **512**, A7
 Acharyya, K., & Herbst, E. 2015, [ApJ](#), **812**, 142
 Ahmadi, A., Beuther, H., Mottram, J. C., et al. 2018, [A&A](#), **618**, A46
 Arellano-Córdova, K. Z., Esteban, C., García-Rojas, J., & Méndez-Delgado, J. E. 2020, [MNRAS](#), **496**, 1051
 Asplund, M., Grevesse, N., Sauval, A. J., & Scott, P. 2009, [ARA&A](#), **47**, 481
 Balser, D. S., Rood, R. T., Bania, T. M., & Anderson, L. D. 2011, [ApJ](#), **738**, 27
 Bayet, E., Awad, Z., & Viti, S. 2010, [ApJ](#), **725**, 214
 Beltrán, M. T., Cesaroni, R., Neri, R., & Codella, C. 2011, [A&A](#), **525**, A151
 Beltrán, M. T., Cesaroni, R., Neri, R., et al. 2005, [A&A](#), **435**, 901
 Brand, J., & Wouterloot, J. G. A. 2007, [A&A](#), **464**, 909
 Browning, M. K., Tumlinson, J., & Shull, J. M. 2003, [ApJ](#), **582**, 810
 Ceccarelli, C., Caselli, P., Bockelée-Morvan, D., et al. 2014, in *Protostars and Planets VI*, ed. H. Beuther et al. (Tucson, AZ: Univ. Arizona Press), 859
 Cesaroni, R. 2005, in *IAU Symp. 227, Massive Star Birth: A Crossroads of Astrophysics*, ed. R. Cesaroni et al. (Cambridge: Cambridge Univ. Press), 59
 Chen, C. H. R., Indebetouw, R., Chu, Y.-H., et al. 2010, [ApJ](#), **721**, 1206
 Chin, Y. N., Henkel, C., Millar, T. J., Whiteoak, J. B., & Mauersberger, R. 1996, [A&A](#), **312**, L33
 Churchwell, E., & Walmsley, C. M. 1975, [A&A](#), **38**, 451
 Churchwell, E., Walmsley, C. M., & Cesaroni, R. 1990, [A&AS](#), **83**, 119
 Cioni, M.-R. L., Clementini, G., Girardi, L., et al. 2011, [A&A](#), **527**, A116
 Coutens, A., Vastel, C., Hincelin, U., et al. 2014, [MNRAS](#), **445**, 1299
 D'Hendecourt, L. B., Allamandola, L. J., Grim, R. J. A., & Greenberg, J. M. 1986, [A&A](#), **158**, 119
 Dufour, R. J. 1975, [ApJ](#), **195**, 315
 Dufour, R. J. 1984, in *IAU Symp. 108, Structure and Evolution of the Magellanic Clouds*, ed. S. van den Bergh & K. S. D. de Boer (Dordrecht: Reidel), 353
 Ellingsen, S. P., Breen, S. L., Caswell, J. L., Quinn, L. J., & Fuller, G. A. 2010, [MNRAS](#), **404**, 779
 Esteban, C., & García-Rojas, J. 2018, [MNRAS](#), **478**, 2315
 Fernández-Martín, A., Pérez-Montero, E., Vilchez, J. M., & Mampaso, A. 2017, [A&A](#), **597**, A84
 Furuya, K., van Dishoeck, E. F., & Aikawa, Y. 2016, [A&A](#), **586**, A127

Garay, G., & Lizano, S. 1999, *PASP*, **111**, 1049

Gensheimer, P. D., Mauersberger, R., & Wilson, T. L. 1996, *A&A*, **314**, 281

Gerakines, P. A., Whittet, D. C. B., Ehrenfreund, P., et al. 1999, *ApJ*, **522**, 357

Goldsmith, P. F., & Langer, W. D. 1978, *ApJ*, **222**, 881

Goldsmith, P. F., & Langer, W. D. 1999, *ApJ*, **517**, 209

Gruendl, R. A., & Chu, Y. 2009, *ApJS*, **184**, 172

Heikkilä, A., Johansson, L. E. B., & Olofsson, H. 1997, *A&A*, **319**, L21

Helmich, F. P., van Dishoeck, E. F., & Jansen, D. J. 1996, *A&A*, **313**, 657

Henize, K. G. 1956, *ApJS*, **2**, 315

Herbst, E., & van Dishoeck, E. F. 2009, *ARA&A*, **47**, 427

HERITAGE Team 2013, Herschel Inventory of the Agents of Galaxy Evolution, IPAC, doi:10.26131/IRSA76

Hernández-Hernández, V., Zapata, L., Kurtz, S., & Garay, G. 2014, *ApJ*, **786**, 38

Herpin, F., Chavarría, L., Jacq, T., et al. 2016, *A&A*, **587**, A139

Hofner, P., Kurtz, S., Churchwell, E., Walmsley, C. M., & Cesaroni, R. 1996, *ApJ*, **460**, 359

Imai, H., Katayama, Y., Ellingsen, S. P., & Hagiwara, Y. 2013, *MNRAS*, **432**, L16

Immer, K., Reid, M. J., Menten, K. M., Brunthaler, A., & Dame, T. M. 2013, *A&A*, **553**, A117

Jacq, T., Walmsley, C. M., Henkel, C., et al. 1990, *A&A*, **228**, 447

Jensen, S. S., Jørgensen, J. K., Furuya, K., Haugbølle, T., & Aikawa, Y. 2021, *A&A*, **649**, A66

Jørgensen, J. K., Belloche, A., & Garrod, R. T. 2020, *ARA&A*, **58**, 727

Jørgensen, J. K., Visser, R., Sakai, N., et al. 2013, *ApJL*, **779**, L22

Karska, A., Herpin, F., Bruderer, S., et al. 2014, *A&A*, **562**, A45

Karska, A., Kaufman, M. J., Kristensen, L. E., et al. 2018, *ApJS*, **235**, 30

Kaufman, M. J., Hollenbach, D. J., & Tielens, A. G. G. M. 1998, *ApJ*, **497**, 276

Knöldlseder, J. 2013, in *Cosmic Rays in Star-Forming Environments*, ed. D. F. Torres & O. Reimer (Berlin: Springer), 169

Koornneef, J. 1984, in *IAU Symp. 108, Structure and Evolution of the Magellanic Clouds*, ed. S. van den Bergh & K. S. D. de Boer (Dordrecht: Reidel), 333

Kristensen, L. E., van Dishoeck, E. F., Mottram, J. C., et al. 2017, *A&A*, **605**, A93

Kuchar, T. A., & Bania, T. M. 1994, *ApJ*, **436**, 117

Kurtz, S., Cesaroni, R., Churchwell, E., Hofner, P., & Walmsley, C. M. 2000, *Protostars and Planets IV* (Tucson, AZ: Univ. Arizona Press), 299

Lazendic, J. S., Whiteoak, J. B., Klamer, I., Harbison, P. D., & Kuiper, T. B. H. 2002, *MNRAS*, **331**, 969

Luck, R. E., & Lambert, D. L. 2011, *AJ*, **142**, 136

Maciel, W. J., & Andrievsky, S. 2019, arXiv:1906.01686

Madau, P., & Dickinson, M. 2014, *ARA&A*, **52**, 415

Marseille, M. G., van der Tak, F. F. S., Herpin, F., & Jacq, T. 2010, *A&A*, **522**, A40

McMullin, J. P., Waters, B., Schiebel, D., Young, W., & Golap, K. 2007, in *ASP Conf. Ser.*, 376, *Astronomical Data Analysis Software and Systems XVI*, ed. R. A. Shaw, F. Hill, & D. J. Bell (San Francisco, CA: ASP), 127

Mehlert, D., Noll, S., Appenzeller, I., et al. 2002, *A&A*, **393**, 809

Meixner, M., Gordon, K. D., Indebetouw, R., et al. 2006, *AJ*, **132**, 2268

Meixner, M., Panuzzo, P., Roman-Duval, J., et al. 2013, *AJ*, **146**, 62

Moscadelli, L., Goddi, C., Cesaroni, R., Beltrán, M. T., & Furuya, R. S. 2008, *A&A*, **480**, 793

Müller, H. S. P., Thorwirth, S., Roth, D. A., & Winnewisser, G. 2001, *A&A*, **370**, L49

Müller, S., Roueff, E., Black, J. H., et al. 2020, *A&A*, **637**, A7

Navarrete, F., Galli, P. A. B., & Damineli, A. 2019, *MNRAS*, **487**, 2771

Neill, J. L., Wang, S., Bergin, E. A., et al. 2013, *ApJ*, **770**, 142

Nguyen Luong, Q., Motte, F., Schuller, F., et al. 2011, *A&A*, **529**, A41

Nummelman, A., Bergman, P., Hjalmarson, Å., et al. 2000, *ApJS*, **128**, 213

Oberg, K. I. 2016, *ChRv*, **116**, 9631

Oliveira, J. M., van Loon, J. T., Chen, C.-H. R., et al. 2009, *ApJ*, **707**, 1269

Oliveira, J. M., van Loon, J. T., Sewilo, M., et al. 2019, *MNRAS*, **490**, 3909

Oliveira, J. M., van Loon, J. T., Sloan, G. C., et al. 2011, *MNRAS*, **411**, L36

Oliveira, J. M., van Loon, J. T., Stanimirović, S., & Zijlstra, A. A. 2006, *MNRAS*, **372**, 1509

Olmi, L., Cesaroni, R., & Walmsley, C. M. 1996, *A&A*, **307**, 599

Palau, A., Fuente, A., Girart, J. M., et al. 2011, *ApJL*, **743**, L32

Pei, Y. C., Fall, S. M., & Hauser, M. G. 1999, *ApJ*, **522**, 604

Persson, M. V., Jørgensen, J. K., van Dishoeck, E. F., & Harsono, D. 2014, *A&A*, **563**, A74

Pickett, H. M., Poynter, R. L., Cohen, E. A., et al. 1998, *JQSRT*, **60**, 883

Pietrzyński, G., Graczyk, D., Gieren, W., et al. 2013, *Natur*, **495**, 76

Reid, M. J., Menten, K. M., Brunthaler, A., et al. 2014, *ApJ*, **783**, 130

Reid, M. J., Menten, K. M., Brunthaler, A., et al. 2019, *ApJ*, **885**, 131

Robitaille, T., & Bressert, E. 2012, *APLpy: Astronomical Plotting Library in Python*, Astrophysics Source Code Library, ascl:1208.017

Robitaille, T. P. 2017, *A&A*, **600**, A11

Robitaille, T. P., Whitney, B. A., Indebetouw, R., & Wood, K. 2007, *ApJS*, **169**, 328

Rolffs, R., Schilke, P., Wyrowski, F., et al. 2011, *A&A*, **527**, A68

Rollestone, W. R. J., Trundle, C., & Dufton, P. L. 2002, *A&A*, **396**, 53

Roman-Duval, J., Gordon, K. D., Meixner, M., et al. 2014, *ApJ*, **797**, 86

Rudolph, A. L., Fich, M., Bell, G. R., et al. 2006, *ApJS*, **162**, 346

Ruffle, D. P., & Herbst, E. 2001, *MNRAS*, **324**, 1054

Russell, S. C., & Dopita, M. A. 1992, *ApJ*, **384**, 508

Rygl, K. L. J., Brunthaler, A., Sanna, A., et al. 2012, *A&A*, **539**, A79

SAGE Team 2006, Surveying the Agents of a Galaxy's Evolution, IPAC, doi:10.26131/IRSA404

Sandell, G., Wright, M., & Forster, J. R. 2003, *ApJL*, **590**, L45

Sanna, A., Reid, M. J., Menten, K. M., et al. 2014, *ApJ*, **781**, 108

Sato, M., Reid, M. J., Brunthaler, A., & Menten, K. M. 2010, *ApJ*, **720**, 1055

Scalise, E. J., & Braz, M. A. 1981, *Natur*, **290**, 36

Scalise, E. J., & Braz, M. A. 1982, *AJ*, **87**, 528

Schmiedeke, A., Schilke, P., Möller, T., et al. 2016, *A&A*, **588**, A143

Schlutheis, M., Rich, R. M., Origlia, L., et al. 2019, *A&A*, **627**, A152

Schwarz, K. R., Ott, J., Meier, D., & Claussen, M. 2012, *AAS Meeting*, **219**, 341.04

Seale, J. P., Looney, L. W., Chen, C. H. R., Chu, Y.-H., & Gruendl, R. A. 2011, *ApJ*, **727**, 36

Seale, J. P., Looney, L. W., Chu, Y.-H., et al. 2009, *ApJ*, **699**, 150

Seale, J. P., Meixner, M., Sewilo, M., et al. 2014, *AJ*, **148**, 124

Sewilo, M., Charnley, S. B., Schilke, P., et al. 2019, *ESC*, **3**, 2088

Sewilo, M., Cordiner, M., Charnley, S. B., et al. 2022, *ApJ*, **931**, 102

Sewilo, M., Indebetouw, R., Charnley, S. B., et al. 2018, *ApJL*, **853**, L19

Shimonishi, T., Dartois, E., Onaka, T., & Boulanger, F. 2016a, *A&A*, **585**, A107

Shimonishi, T., Das, A., Sakai, N., et al. 2020, *ApJ*, **891**, 164

Shimonishi, T., Izumi, N., Furuya, K., & Yasui, C. 2021, *ApJ*, **922**, 206

Shimonishi, T., Onaka, T., Kato, D., et al. 2008, *ApJL*, **686**, L99

Shimonishi, T., Onaka, T., Kato, D., et al. 2010, *A&A*, **514**, A12

Shimonishi, T., Onaka, T., Kawamura, A., & Aikawa, Y. 2016b, *ApJ*, **827**, 72

Skrutskie, M. F., Cutri, R. M., Stiening, R., et al. 2006, *AJ*, **131**, 1163

Suutarien, A. N., Kristensen, L. E., Mottram, J. C., Fraser, H. J., & van Dishoeck, E. F. 2014, *MNRAS*, **440**, 1844

van der Tak, F. F. S., Chavarría, L., Herpin, F., et al. 2013, *A&A*, **554**, A83

van der Tak, F. F. S., Walmsley, C. M., Herpin, F., & Ceccarelli, C. 2006, *A&A*, **447**, 1011

van Dishoeck, E. F., Kristensen, L. E., Mottram, J. C., et al. 2021, *A&A*, **648**, A24

van Loon, J. T. 2012, arXiv:1210.0983

van Loon, J. T., Hekkert, P. T. L., Bujarrabal, V., Zijlstra, A. A., & Nyman, L.-A. 1998, *A&A*, **337**, 141

van Loon, J. T., Oliveira, J. M., Gordon, K. D., Sloan, G. C., & Engelbracht, C. W. 2010a, *AJ*, **139**, 1553

van Loon, J. T., Oliveira, J. M., Gordon, K. D., et al. 2010b, *AJ*, **139**, 68

van Loon, J. T., Oliveira, J. M., Wood, P. R., et al. 2005, *MNRAS*, **364**, L71

van Loon, J. T., & Zijlstra, A. A. 2001, *ApJL*, **547**, L61

van Loon, J. T., Zijlstra, A. A., Bujarrabal, V., & Nyman, L. Å. 2001, *A&A*, **368**, 950

Wang, M., Chin, Y.-N., Henkel, C., Whiteoak, J. B., & Cunningham, M. 2009, *ApJ*, **690**, 580

Welty, D. E., Federman, S. R., Gredel, R., Thorburn, J. A., & Lambert, D. L. 2006, *ApJS*, **165**, 138

Westerlund, B. E. 1997, in *The Magellanic Clouds*, ed. B. E. Westerlund (Cambridge: Cambridge Univ. Press), 292

Whiteoak, J. B., & Gardner, F. F. 1986, *MNRAS*, **222**, 513

Whiteoak, J. B., Wellington, K. J., Jauncey, D. L., et al. 1983, *MNRAS*, **205**, 275

Wright, M., Zhao, J.-H., Sandell, G., et al. 2012, *ApJ*, **746**, 187

Wu, J., Evans, N. J. I., Gao, Y., et al. 2005, *ApJL*, **635**, L173

Xu, Y., Moscadelli, L., Reid, M. J., et al. 2011, *ApJ*, **733**, 25

Zhang, B., Moscadelli, L., Sato, M., et al. 2014, *ApJ*, **781**, 89